Image-based Dose Correlation Studies on Radiation-induced Lung Injury

Sangkyu Lee

Master of Science

Medical Physics Unit

McGill University

Montreal, Quebec

August 2010

A thesis submitted to McGill University in partial fulfillment of the requirements of the degree of Master of Science in Medical Radiation Physics

ABSTRACT

The goal of this work is to develop an accurate and automatic tool to evaluate normal lung tissue response to radiotherapy (RT) and its correlation with local dose. Manifestation of radiation-induced lung disease (RILD) in radiography is a measurable endpoint for RT-induced normal tissue complication. Follow-up CT images from RT-received non-small-cell lung cancer patients were registered to a corresponding planning CT image. Following image intensity calibration, the extent of RILD was segmented based on the change in physical density during the follow-up period. Dose coverage to the RILD segmentation and healthy lung was calculated based on retrieved treatment plans. Normal tissue response in terms of RILD volume and local dose-response showed significant dependency on patients and follow-up periods. Monte-Carlo dose calculation was found to be important to obtain better correlation. Provided the improved accuracy in CT calibration and image registration, this tool can facilitate further normal tissue toxicity studies.

ABRÉGÉ

Le but de ce travail est de développer un outil automatisé de haute précision permettant dévaluer la réponse de tissus de poumons sains à la radiothérapie (RT), ainsi que leurs corrélation avec la dose locale. Les complications de tissus de poumons sains induites par RT peuvent être mesurées à laide des manifestations de maladies pulmonaires induites par radiations (MPIR) en radiographie. Le suivi des images CT par des cellules de poumons cancéreuses provenant de la RT a été enregistré à leur image CT de planification correspondante. à l'aide du suivi de la calibration de lintensité de limage, létendue des MPIR a été segmentée en se basant sur le changement de densité physique durant la période de suivi. La dose reliée à la segmentation des MPIR et aux tissus de poumons sains a été calculée en se basant sur des planifications de traitements établis. La réponse des tissus sains en termes de volume MPIR et la réponse de la dose locale ont démontrées une dépendance significative par rapport aux patients et aux périodes de suivi. Le calcul de dose par simulations Monte-Carlo sest révélé être important afin dobtenir de meilleures corrélations. En tenant compte de lamélioration de lexactitude des calibrations CT et des enregistrements d'image, cet outil peut faciliter le déroulement des futures études de toxicité des tissus sains.

ACKNOWLEDGEMENTS

First, I would like to thank my thesis supervisors, Dr. Jan Seuntjens and Dr. Gabriela Stroian, for their guidance, inspiration, and financial support. I also wish to acknowledge the contribution from the two oncologists at the Montreal General Hospital (MGH), Dr. Sergio Faria M.D. and Dr. Luis Souhami M.D., who initiated this study with Jan and provided patient data.

My work on patient dose calculation would have been impossible without the help from Andrew Alexander who provided and updated his software and patiently answered my questions related to the Monte-Carlo methods. Also, I would like to thank Dr. Louis Collins for his innovative image registration tool and Dr. Emily Heath for valuable e-mail discussions on image registration problems. Many thanks to Dr. Issam El Naqa, who recently joined McGill faculty but contributed significantly to this work by sharing his extensive knowledge in radiation toxicity studies.

I would like to appreciate Dr. Ervin Podgorsak for developing this excellent graduate program. His lectures during the first year were important for me to conduct research under a firm theoretical background in medical physics. I am also grateful to all the medical physicists at the MGH for their supports in the clinic and valuable comments on my work at research meetings and Friday morning talks. I thank Martin Carrier-Vallieres for translating the abstract and all the other fellow students for making my study in Montreal enjoyable.

My final gratitude is dedicated to my parents and brother for their infinite love.

TABLE OF CONTENTS

ABSTRACT i

ABRÉGÉ ii

ACKNOWLEDGEMENTS iii

LIST OF FIGURES vii

LIST OF TABLES x

1 Introduction 1

1.1 Radiotherapy for lung cancer 1
1.2 Brief review on radiobiology 3
1.3 Overview of radiation-induced lung disease (RILD) 5
1.3.1 Acute damage 5
1.3.2 Late damage 6
1.4 Quantification of RILD: measurable endpoints 9
1.4.1 CT densitometry 9
1.4.2 Pulmonary function test 10
1.4.3 Perfusion scan 10
1.4.4 Clinical syndromes 11
1.4.5 Others 11
1.5 Risk factors for RILD 11
1.5.1 Irradiation technique 11
1.5.2 Chemotherapy 12
1.5.3 Genes 12
1.5.4 Others 12
1.6 Risk assessment of RILD 13
1.7 Scope of this project 15
1.8 Thesis objectives 16
1.8.1 Thesis organization 16

2 Image Registration 18

2.1 Introduction 18
2.2 Classification 20
2.2.1 Linear registration 20
2.2.2 Deformable registration 23
2.3 Similarity metrics 27

2.3.1 Voxel-based metrics . . . 27
2.3.2 Geometry-based metrics . . . 28
2.3.3 Statistics-based metrics . . . 29
2.4 Optimization method . . . 30
2.5 Validation of registration . . . 32
2.5.1 Landmark-based validation . . . 32
2.5.2 Similarity metrics . . . 32
2.5.3 Contour matching . . . 33

3 Materials and Methods . . . 34

3.1 Overview . . . 34
3.2 Subjects . . . 34
3.3 Patient data . . . 35
3.3.1 Images . . . 35
3.3.2 Treatment plans . . . 36
3.4 Beam models . . . 36
3.5 Image registration . . . 36
3.5.1 Registration software . . . 36
3.5.2 Choice of registration algorithm . . . 37
3.5.3 Pre-registration steps . . . 37
3.5.4 Transformation optimization . . . 38
3.5.5 Post-registration processing . . . 40
3.5.6 Verification . . . 40
3.6 Intensity calibration . . . 42
3.6.1 CT calibration . . . 42
3.7 Lung and injury segmentation . . . 44
3.7.1 Lung segmentation . . . 44
3.7.2 Injury segmentation . . . 46
3.8 Dose calculation . . . 46
3.8.1 Calculation by AAA . . . 47
3.8.2 Calculation by MC . . . 47
3.9 Dose-injury correlation study . . . 52

4 Results . . . 53

4.1 overview . . . 53
4.2 Image registration . . . 53
4.3 RILD segmentation . . . 53
4.4 Dose calculation . . . 55
4.5 Post-RT dependence of RILD volume . . . 56
4.6 RILD-local dose correlation . . . 56
4.7 Strength of correlation . . . 58
4.8 Uncertainty analysis . . . 59
4.9 Summary . . . 60

5 Discussion 65

6 Conclusions and Outlook 71

A Uncertainty Analysis 73

A.1 Overview 73
A.2 Image registration 73
A.3 CT calibration 74
A.4 Dose calculation (MC dose only) 75
A.5 Total uncertainty 75

LIST OF FIGURES

Figure		page
1.1	Dose-response relationship for early and late-responding tissues.	4
1.2	Dose-response relationship for tumor control and normal tissue complication.	5
1.3	Ground-glass opacity of radiation pneumonitis.	7
1.4	Three distinct patterns of pulmonary fibrosis induced by three-dimensional conformal radiotherapy (3D-CRT).	8
1.5	FDG-PET uptake in post-radiation pneumonitis.	10
2.1	Overview of image registration involving correspondence determination, coordinate system transformation, resampling and interpolation.	19
2.2	Illustration showing the improvement of similarity by nonlinear registration.	24
3.1	Block diagram illustrating the workflow of the analysis.	34
3.2	Pre-registration image processing.	39
3.3	Change in image similarity in terms of cross correlation during multi-resolutional optimization.	40
3.4	Measurement of in-slice DTA which evaluates the average displacement between planning CT (yellow) and post-RT (blue) lung contours.	41
3.5	Conversion of planning CT numbers to physical density.	44
3.6	Scatter plot of the two slopes (x-axis) and corresponding intercepts (y-axis) of the CT calibration functions for 6 scanner models.	45
3.7	Flowchart of a MC simulation of photon transport.	48
3.8	Flowchart of the processes to obtain a phase-space file in the BEAMnrc platform.	49

3.9 Comparison of percent depth dose along the central axis between ion-chamber measurement and Monte-Carlo simulation of a 10 × 10 cm photon beam from the Varian Clinac 21 X linear accelerator. 50

3.10 Comparison of dose profiles at the depth of dose maximum between ion-chamber measurement and Monte-Carlo simulation of a 10 × 10 cm photon beam from the Varian Clinac 21 X linear accelerator. 51

4.1 Example of affine registration showing anisotropic registration accuracy. Lung volumes from a target image (yellow) and a registered source image (dark red) are overlayed in a coronal (top) and a sagittal (bottom) view. 54

4.2 Injury segmentation (shown in purple) based on the physical density difference between the planning CT (top left: PTV contoured in red) from the post-RT CT (top right) included the small and isolated mis-aligned voxels which are clearly distinguishable from radiation pneumonitis in right-posterior lung (bottom left). Interactive correction on injury segmentation produced the final injury segmentation (bottom right). 55

4.3 Changes of the volume of the scored RILD in ipsilateral (top) and contralateral (bottom) lung as a function of post-RT time for all patients. 57

4.4 Dose-response curves for ipsilateral (red) and contralateral (blue) lung of patient 1. Figure 4.4 ∼ Figure 4.8: Correlation with MC and AAA dose shown in straight and dotted lines, respectively. Error bars are combined uncertainties (see the appendix). Asterisks(*) denote the dose bins where the probability obtained from MC dose is significantly different from AAA dose. 62

4.5 Dose-response curves for ipsilateral (red) and contralateral (blue) lung of patient 2. 63

4.6 Dose-response curves for ipsilateral lung of patient 3. No injury was found in contralateral lung. 63

4.7 Dose-response curves for ipsilateral lung of patient 4. No injury was found in contralateral lung. 64

4.8 Dose-response curves for ipsilateral lung of patient 5. No injury was found in contralateral lung. 64

5.1 Comparison of the performance of affine against deformable (optical flow) registration using algorithm under the presence of pneumonitis volume. 68

A.1 Demonstration of the change of a dose-response curve due to the shift of dose distribution by registration accuracy. 74

A.2 Demonstration of the change of one dose-response curve due to the uncertainty in calibrated physical density. 76

LIST OF TABLES

Table		page
1.1	RTOG/EORTC acute radiation morbidity scoring criteria for lung.	6
1.2	RTOG/EORTC late radiation morbidity scoring criteria for lung.	7
2.1	Comparison of registration models in section 2.2.	26
3.1	Survey of 5 patients observed for the study.	35
3.2	6 scanner models as identified from DICOM headers.	45
4.1	Distance-to-agreement (DTA) between ipsilateral (ipsi.) and contralateral (cont.) lung contours drawn on a planning CT image and registered post-treatment (Post1∼Post5) CT images.	54
4.2	Average dose to the segmented ipsilateral (ipsi) and contralateral (cont) lung using MC or AAA calculation engines. Dose uncertainties from MC (unc.) and MC-AAA difference are shown in percentage of MC dose value.	56
4.3	Spearman's coefficients (r_s) and associated p-values for local injury-dose correlation from all patients, classified into the three observation periods (early, intermediate, and late).	58
4.4	Spearman's coefficients (r_s) and associated p-values for local injury-dose correlation for each of 5 patients.	59
4.5	Statistics of uncertainties on $P(D_i)$ from the three main sources. Numbers shown in percentage complication probability.	60

CHAPTER 1
Introduction

1.1 Radiotherapy for lung cancer

Lung cancer is one of the most significant health concerns in Canada: its incidence was 23,400 in 2009 with the 5-year survival ratio of 15% being the second lowest of all cancer types [1]. External beam radiotherapy, the use of ionizing radiation to induce the killing of cancerous cells, has still been widely used in lung cancer treatment due to its non-invasive nature. Approximately 61% of lung cancer patients are referred for radiotherapy [2]. However, radiation sequelae resulting from inevitable irradiation of normal tissue occur quite frequently and negatively affect the survival of a patient after the therapy. Hence, the goal of any radiotherapy is twofold: maximizing tumour control and minimizing toxicity to normal tissues surrounding the tumour. Success of radiotherapy ultimately depends on delivering as much radiation as possible to a target and as little radiation as possible to its surroundings. This requires: i) a careful treatment planning based on the actual 3D image of an area to be treated, and ii) radiation delivery technique which can conform homogeneous irradiation to a target volume.

The introduction of computed tomography (CT) revolutionized radiotherapy in a way that it enabled 3D imaging and thereby 3D dose calculation on a patient. A treatment plan is created on a simulation (planning) CT image which is obtained prior to the treatment. On the simulation CT image, the extent of a disease is delineated based on the judgements of physicians and named as a clinical target volume (CTV). Then, the spatial uncertainty of

the positioning of the tumour during the course of dose delivery is added onto the CTV usually as a few centimeters of isotropic margin. The CTV with the margin is called a planning target volume (PTV) to which a prescribed radiation dose will be delivered.

Techniques in radiotherapy have evolved to enhance the conformity of radiation field to the PTV. Three-dimensional conformal radiotherapy (3D-CRT) is a widely used technique to fit the shape of a radiation field to the projection of the 3D image of a tumor. However, more complex treatment planning is required when radiosensitive organs in the vicinity of the tumor need to be spared. Recently, Intensity-modulated radiation therapy (IMRT) was introduced to optimize treatment planning in terms of dose conformity as well as sparing of the organs at risk. The optimized plan is fed into a physical delivery system in which the intensity of radiation is modulated in multiple small volumes. IMRT is often used in the treatment of head and neck cancer where the sparing of radiosensitive organs such as salivary gland and optic nerves is desired. However, the application to lung is still immature due to respiratory motion during the delivery [3].

Typically, radiation dose is given through several fractions over a period of a month or two. So far, it has been assumed that patient anatomy does not significantly change through the course of treatment. As a result, the treatment plan created before the first day of treatment is altered only for the position of the isocenter. The new position for the isocenter is determined based on the locations of fiducial markers [1] implanted on a patient body or anatomical structures from on-board images which are obtained from the X-ray imagers incorporated into a treatment machine. The patient anatomy is never static, however, either on a short (breathing) or long (weight loss, tumour growth/shrinkage) time scale. A concept of adaptive radiotherapy (ART)

requires an image feedback system that re-contours a target and organs at risk on a daily CT image taken prior to each fraction and update the treatment plan and delivery based on the new contours. Adaptation of treatment in response to patient/organ temporal variation could improve the outcome of the treatment by both maximizing conformity and reducing the amount of normal tissues to be irradiated.

1.2 Brief review on radiobiology

Biological effects produced by ionizing radiation are principally attributed to damage on deoxyribonucleic acid (DNA) by ions or free radicals set in motion by the radiation. DNA damage, if it exceeds the capacity for self-repair, leads to the loss of the reproductive integrity of a cell, and eventually, cell death. The relationship between cell survival and radiation dose, deposited energy per unit mass, is well established by experiments and represented by the linear quadratic relationship:

$$S = e^{-\alpha D - \beta D^2} \tag{1.1}$$

in which S is the fraction of cells surviving a dose D, and α and β are constants representing the linear and quadratic components of cell killing. A ratio α/β determines the curvedness of a survival curve and is an important parameter to characterize the radiosensitivity of a tissue. Tissues that divide rapidly such as tumor cells respond to radiation earlier than normal tissues, which translate into a larger α/β ratio (figure 1.1). Higher radiosensitivity of tumor cells than normal tissues is the fundamental paradigm for the use of

[1] Fiducial markers are implants fixed on the skin of a patient to set a reference plane/point for patient positioning at each fraction. Normally they are metallic needles distinguishable from fat or soft tissue on X-ray or CT images.

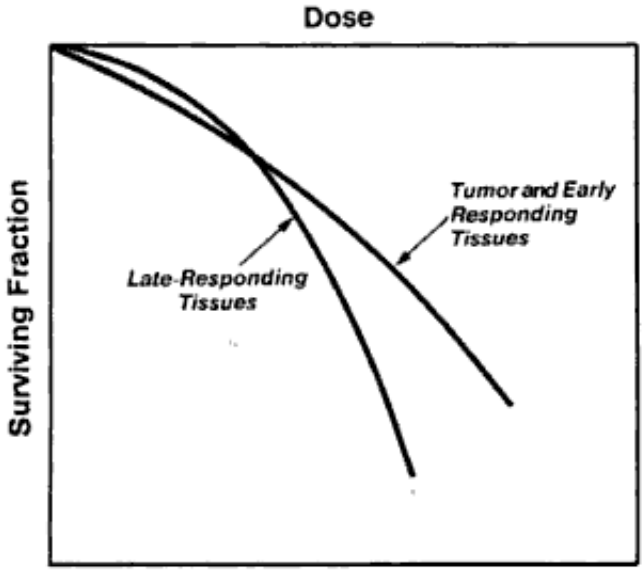

Figure 1.1: The dose-response relationship for late-responding tissue is more curved than for early-responding tissues. In the linear-quadratic formulation, this translates into a larger α/β ratio for early effects than for late effects. Reproduced from [4].

ionizing radiation for cancer treatment. Depopulation of cells leads to functional alteration in tissues which consequence would be the loss of malignancy (tumor control) for tumors or the loss of function (normal tissues). Relation between the incidence of those alterations and radiation dose is demonstrated in dose-response curves. Such dose-response curves have a sigmoid (S) shape (figure 1.2).

Apparent radioresponsiveness of a tissue depends on inherent sensitivity of cells, kinetics of the tissue or cell population, and the way cells are organized in that tissue. An organ system consists of several types of tissues with different radioresponsiveness and patterns of response. Thus, radiation effects to organs are generally biphasic: early and late. Early, or acute, effects result from the death of a large number of cells and occur within a few days or weeks of irradiation in tissues with rapid turnover rate. Late effects appear after

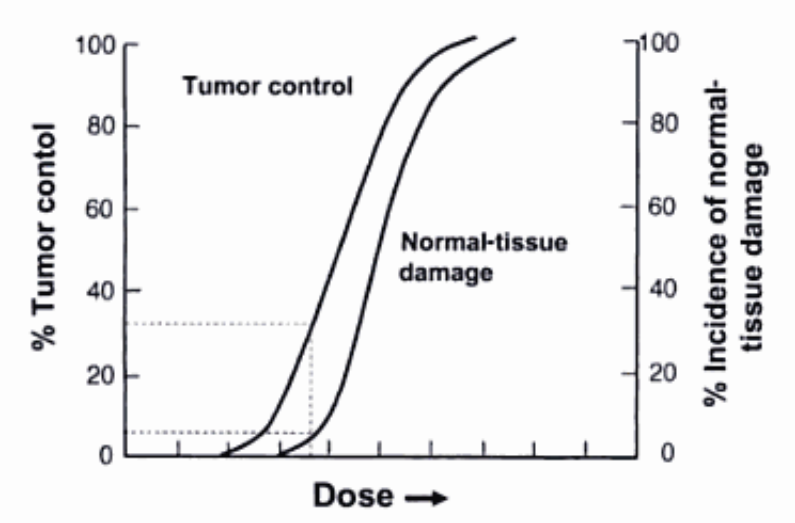

Figure 1.2: The dose-response relationship is sigmoid in shape for both tumor control and normal-tissue damage. The response curve for the tumor control is on the left to a curve for normal tissue, showing higher radiosensitivity for tumors. Reproduced from [4].

a delay of months or years and occur predominantly in slowly proliferating tissues.

1.3 Overview of radiation-induced lung disease (RILD)

External beam radiotherapy (RT) on tumor sites in thorax (e.g. lung, breast, esophagus, Hodgkin's disease) is a major iatrogenic cause for RILD. Similarly to other radiation effects on normal tissues, RILD is broadly divided into acute (early) and late damage.

1.3.1 Acute damage

Early (Acute) radiation change typically occurs within 3 months after the completion of RT. The most significant change is radiation pneumonitis (RP) which is characterized by cellular infiltration that mainly consists of macrophages. Pneumonitis is a direct consequence of the damage to alveoli and capillaries, particularly type II pneumocytes of the alveoli, and the resultant release of pulmonary surfactant [5]. Biological mechanism for the sequence of these events is unknown, but might result from a radiation-induced cytokine

Grade	Description
1	Mild symptoms of dry cough or dyspnea on exertion
2	Persistent cough requiring narcotic, antitussive agents/dyspnea with minimal effort but not at rest
3	Severe cough unresponsive to narcotic antitussive agent or dyspnea at rest/clinical or radiological evidence of acute pneumonitis/intermittent oxygen or steroids may be required
4	Severe respiratory insufficiency/continuous oxygen or assisted ventilation
5	fatal

Table 1.1: RTOG/EORTC acute radiation morbidity scoring criteria for lung.

cascade [6]. Pneumonitis often accompanies pleural effusion (fluid accumulation in a pleural sac) [7]. Symptomatic pneumonitis involves cough, fever, and dyspnea (shortness of breath). The severity of pneumonitis is graded into four classes according to the criteria presented by the Radiation Therapy Oncology Group (RTOG) and the European Organization for Research and Treatment of Cancer (EORTC) (table 1.1) [8]. Radiation pneumonitis is radiologically identified as a ground-glass opacity in an area immediately around the tumor [9] (figure 1.3).

1.3.2 Late damage

Late damage in lung due to radiation begins usually between 6 to 12 months and becomes stable after 2 years. One of the marked alterations in lung parenchyma is the deposition of collagenous scar tissue which is referred to as radiation fibrosis. Fibrosis is understood as a consequence of the prolonged action of molecular stimuli for pneumonitis: a popular theory is that persistent production of cytokines activates the genes for growth factors such as TNF-α and TGF-β, which in turn leads to accumulation of collagenous tissues [5] [6]. Radiation fibrosis results in decreased lung capacity and lung compliance, and its exacerbation might require assisted ventilation. As for

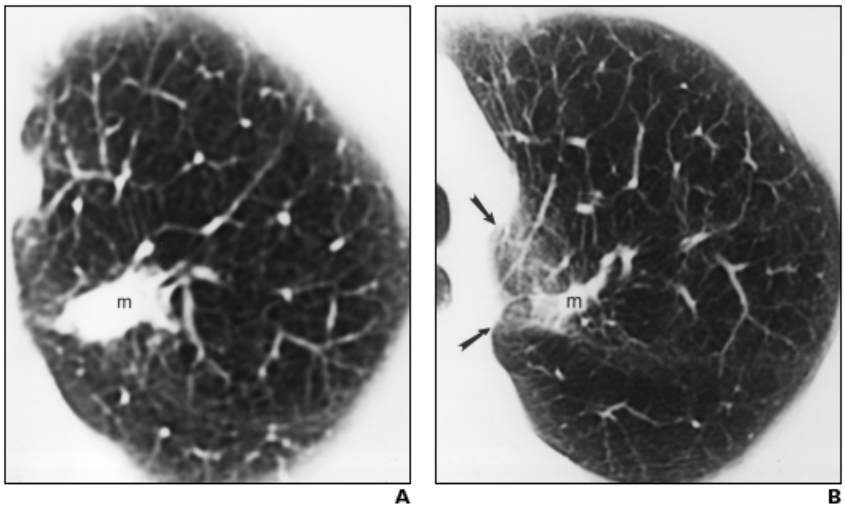

Figure 1.3: Ground-glass opacity of radiation pneumonitis from a lung cancer patient by [10]. A: pre-RT computed tomography (CT) scan with a tumor mass marked as m, B: CT scan obtained 5 weeks after completion of RT shows ground-glass opacities adjacent to the tumor site.

early toxicity, RTOG and EORTC presented symptomatic criteria for grading radiation fibrosis (table 1.2) [8]. Radiological manifestation of radiation fibrosis has distinct patterns: the patterns of injury induced by conventional RT include consolidation, volume loss, and bronchiectasis (inflated airways), while the 3D-CRT induced patterns can be the conventional patterns with less degree (modified conventional), a scarlike pattern (linear opacity in the region of the original tumour), or a masslike pattern [9] (figure 1.4).

Grade	Description
1	Asymptomatic or mild symptoms (dry cough)
2	Moderate symptomatic fibrosis or pneumonitis (severe cough), low grade fever; patchy radiographic appearances
3	Severe symptomatic fibrosis or pneumonitis; dense radiographic changes
4	Severe respiratory insufficiency/continuous oxygen or assisted ventilation
5	fatal

Table 1.2: RTOG/EORTC late radiation morbidity scoring criteria for lung.

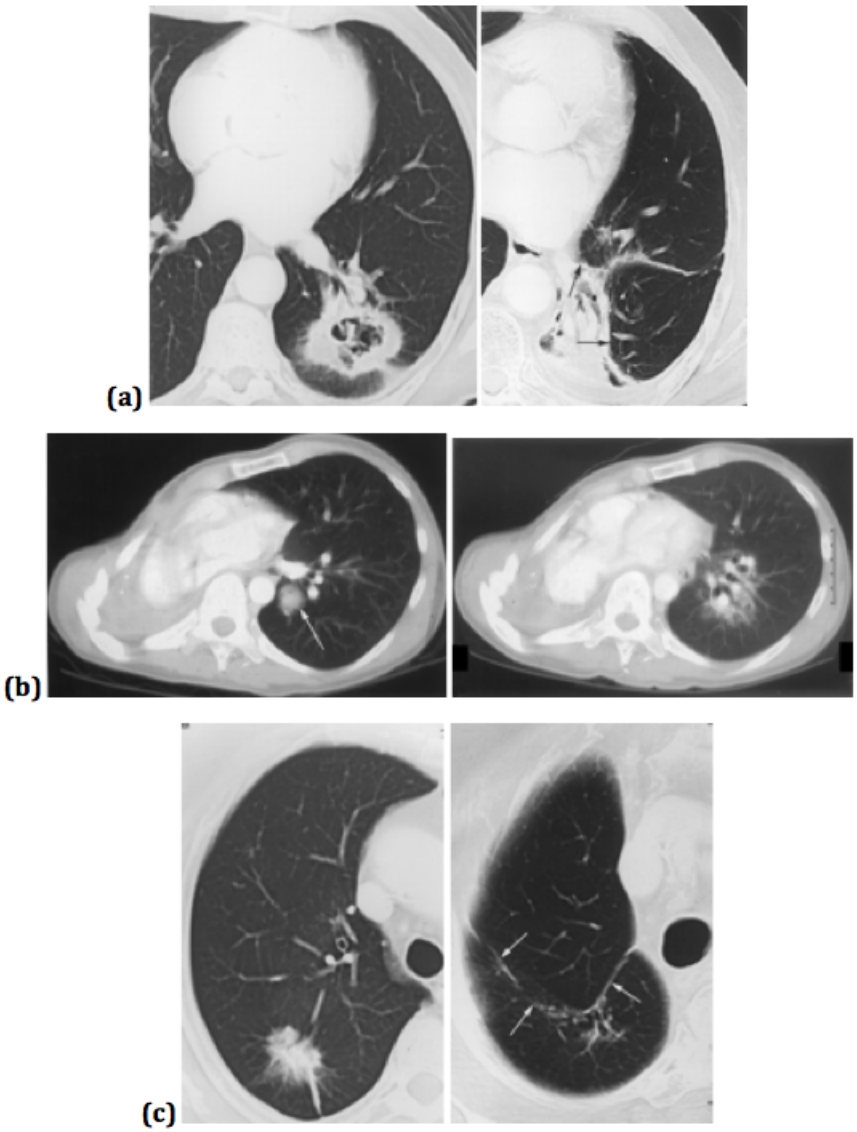

Figure 1.4: Three distinct patterns of pulmonary fibrosis induced by three-dimensional conformal radiotherapy (3D-CRT) [9]. (a) Modified conventional pattern. Left: pre-radiotherapy (RT) CT scan with tumour mass in left lower lobe. Right: CT scan acquired 22 months after RT radiation-induced changes (arrows) which include consolidation, volume loss, and traction bronchietasis. (b) Masslike pattern. Left: pre-RT CT scan with a tumor mass in left lower lobe (arrow). Right: CT scan acquired 21 months after RT exhibiting consolidation and bronchietasis near tumor site. (c) Scarlike pattern. Left: pre-RT CT scan with a lesion in right upper lobe. Right: CT scan acquired 11 months after RT showing linear bands of consolidation (arrows).

1.4 Quantification of RILD: measurable endpoints

1.4.1 CT densitometry

Radiation pneumonitis and fibrosis result in the replacement of lung parenchyma by relatively dense material (exudate or fibrotic tissues), which can be detected by radiographic imaging. Computed tomography (CT) is a non-invasive method to quantitatively measure the extent of RILD. The pixel value of a CT image (CT number) is linearly associated with physical density and their relationship is affected by X-ray energy, scanner type, or beam hardening. CT calibration refers to empirical determination of the relationship between CT number and physical density under the specified conditions.

Literature has reported the increase in average lung density after thoracic irradiation([11],[12],[13]), although it is a quite insensitive index of radiation damage [12]. Regional lung density is alternatively used as a measure for local damage, and correlation with local dose has been shown by Ma et al. [14], Rosen et al. [15], Stroian et al. [16]. Since the direct spatial comparison between CT images before and after the treatment requires image registration, the accuracy of the correlation is subject to that of the registration amongst other parameters.

The presence of other pulmonary abnormalities such as pneumonia, emphysema, and residual or recurrent malignancies can create false positives for the CT-based diagnosis of RILD due to their similar radiographic manifestation. The diagnosis of malignancy by positron emission tomography (PET) imaging with fluoro-2-deoxy-D-glucose (FDG) can help improve the specificity in the diagnosis of RILD by differentiating metabolically active malignant cells from non-active radiation induced damage [17] [18]. However, radiation pneumonitis may show high FDG uptake due to high glucose demand by

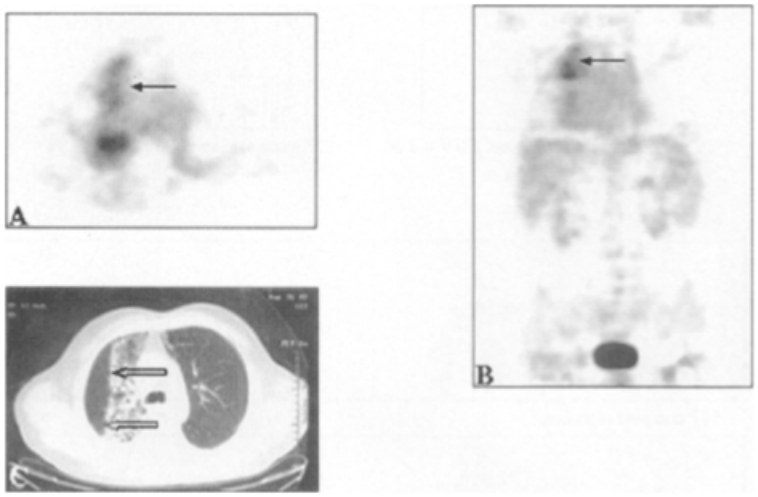

Figure 1.5: An FDG-PET study identifies postradiation pneumonitis [18]. Increased FDG uptake was shown in the medial aspect of a right upper lobe, on the transverse (A) and coronal (B) slices (thin arrow). The corresponding region (open arrow) also manifested as ground-glass opacity in CT (C), which is the radiological characteristic of radiation pneumonitis.

macrophages, which makes the differentiation difficult at the early stage of RILD [17] [18] [19] [20] (figure 1.5).

1.4.2 Pulmonary function test

Pulmonary function tests can assess the impact of RILD on breathing rate, lung capacity, and lung compliance. Increase in breathing rate can occur as a compensatory reaction to impaired pulmonary function and has been reported for animal studies [11]. In human, reductions in diffusion capacity are demonstrated as the decrease in FEV1 (forced expiratory volume), TLC (total lung capacity), and lung compliance in severe cases [21].

1.4.3 Perfusion scan

Another possible endpoint is perfusion inequality which is a consequence of radiation-induced microvascular damage. Single photon emission computed tomography (SPECT) is the most common modality of investigating perfusion in lung. Reduction in regional perfusion is correlated with local radiation

dose [22] but in a different manner than CT density, suggesting that the CT endpoint does not necessarily coincide with the SPECT endpoint [14].

1.4.4 Clinical syndromes

RTOG/EORTC toxicity criteria (table 1.1, table 1.2) are widely accepted in clinical research to grade injuries based on symptoms. Consensus is that the cases of RTOG/EORTC grade 3 or higher is counted as an incidence of symptomatic injury. However, the precision of symptomatic endpoints is often limited by confounding medical conditions, such as tumor regrowth, chronic obstructive pulmonary disease (COPD), and cardiac disease ([23]). A symptomatic endpoint does not necessarily coincide with other endpoints. For example, radiographical findings of radiation pneumonitis are almost always present in patients who received more than 40 Gy [24], whereas the frequency of symptomatic pneumonitis ranges only 0∼20% [25].

1.4.5 Others

In nuclear medicine, gallium lung scanning is used for the detection of inflammatory change within lung parenchyma [26]. Inflammatory reaction can also be detected from a sample of fluid taken from lung interstitium. This technique called lung lavage is an equally effective alternative to lung biopsy [27]. Patients with pneumonitis are shown to exhibit positive results on a lung lavage and gallium scan [28].

1.5 Risk factors for RILD

1.5.1 Irradiation technique

The three main factors of RT techniques associated with the risk of RILD are: i) the total radiation dose, ii) the volume of lung irradiated, and iii) the dose fractionation. Generally, the probability for any radiation-induced disorders generally increases with radiation dose to lung tissues above a certain threshold dose (figure 1.2). The dependency of the complication probability on

irradiated volume is explained by a common view that lung consists of parallel functional subunits (FSU). Dysfunction of so-called parallel function organs is related to the number of damaged FSUs, which increases with irradiated volume [29]. Hypofractionation, the use of greater dose per fraction, is shown to have a detrimental effect on radiation pneumonitis [30]. Mathematical predictive models that incorporate all these irradiation technique factors will be described in a following section.

1.5.2 Chemotherapy

The type of chemotherapy (ChT) agents as well as the type of regimen (e.g. ChT alone, sequential ChT/RT, and concurrent ChT/RT) are associated with pulmonary toxicity. Chemotherapy agents such as bleomycin, busulfan, carmustine (BCNU), and mitomycin-C are reported to have the highest incidence of chemotherapy-induced pulmonary diseases, with the majority of manifestation being pulmonary fibrosis [31]. Clinical investigation by Byhardt et al. [32] found that late lung toxicity with concurrent ChT/RT is significantly greater than sequential ChT/RT.

1.5.3 Genes

The genetic factors that influence congenital susceptibility to RILD have been investigated using mice model [33] [34]. In human, genotype polymorphism in TGF-β1 [35], XRCC1 [36], and ATM [37] genes are shown to be related to variation in patient response to RT. This suggests the use of biomarkers for detecting the expression of these genes as a risk predictor of RILD. However, complexity in RILD pathogenesis still remains as a challenge to these genotyping analyses.

1.5.4 Others

Tumour position in superior-inferior direction is found to be correlated with the RILD incidence more strongly than any single dosimetric parameters

[38] [39]. This suggests the regional dependence of the radiosensitivity of lung is associated with the interaction between pulmonary and cardiac functional deficits [40]. Other clinical variants which are reported to correlate with RILD include age [41], smoking habit [42] [43], weight loss [42], and pulmonary function [22], although the significance of the correlation varies with studies.

1.6 Risk assessment of RILD

Several dosimetric parameters (V_{20}, MLD, NTD, and NTCP) derived from dose-volume histogram (DVH) have been used in the clinic for estimating the risk of complication. V_{30} is defined as the percentage of lung volume receiving more than 30 Gy. MLD (mean lung dose) is calculated as the average dose to lung. NTD (normalized total dose), derived from a linear-quadratic model for dose-response, is a biologically equivalent dose to which a physical dose D is normalized as a function of the number of fraction (n), and biological endpoints (α/β) where D is a physical dose (e.g. MLD) (Eq. 1.2).

$$NTD = \frac{D(1 + \frac{D/n}{\alpha/\beta})}{1 + \frac{2}{\alpha/\beta}} \tag{1.2}$$

NTCP (normal tissue complication probability) is assumed to follow a sigmoid dose-response relationship (Eq. 1.3) where the shape of the sigmoidal function is parametrized by the following empirically-determined variables : $TD_{50}(1)$ (tolerance dose for uniform whole organ irradiation), m (steepness of the dose-response curve), and n (volume dependency of the complication probability) (Eq. 1.4, 1.5). For non-uniform irradiation, DVH is reduced to an equivalent uniform DVH with maximum dose over an effective volume v according to the analytical method by Kutcher and Burman [44].

$$NTCP = \frac{1}{\sqrt{2\pi}} \int_{-\infty}^{t} e^{(-x^2/2)} dx \tag{1.3}$$

$$t = \frac{D - TD_{50}(v)}{m * TD_{50}(v)} \tag{1.4}$$

$$TD_{50}(v) = TD_{50}(1)v^{-n} \tag{1.5}$$

Several studies ([45], [46], [47], [25]) demonstrated the correlation between these DVH-based parameters and the incidence of pneumonitis of RTOG grade 3 or higher. Despite the correlation, the DVH parameters have high rates of false negatives (0 to 50%), low sensitivity (50% to 100%), and low overall accuracy (52% to 81%) [48], which calls for the more accurate prediction model that integrates all the clinically relevant variables besides dosimetric parameters. Some investigators applied statistical learning methodology to build maximally predictive models driven by treatment, anatomical and patient-related information. Hope et al. [38] and El Naqa et al. [49] obtained an optimal pneumonitis risk model using multivariate logistic regression approach where the risk is expected to follow a sigmoidal shape. The logistic model is [50]:

$$P(\mathbf{x_i}) = \frac{e^{g(\mathbf{x_i})}}{1 + e^{g(\mathbf{x_i})}}, i = 1, ..., n, \tag{1.6}$$

where n is the number of cases (patients), $\mathbf{x_i}$ is a vector of the input variable values used to predict $P(\mathbf{x_i})$ for outcome y_i of the i_{th} patient. The "x-axis" summation $g(\mathbf{x_i})$ is given by:

$$g(\mathbf{x_i}) = \beta_0 + \sum_{j=1}^{s} \beta_j x_{ij}, i = 1, ..., n, j = 1, ..., s, \tag{1.7}$$

where s is the number of model variables and the βs are the set of model coefficients that are determined by maximizing the probability that the data give rise to the observations.

1.7 Scope of this project

Structural damage in lung is a necessary, though not sufficient, condition for the deterioration of lung function. Therefore, prediction of RILD risk would be incomplete without a full understanding of structural change. Although RILD is an outcome of complex interactions between numerous variables, univariate analysis is still useful as we know that radiation dose is a primary cause. This study aimed at establishing a link between radiation dose and pulmonary damage that would lead to RILD as assessed with radiographic means by retrospective case studies. CT image voxel-based statistical analysis was a key technique to exploit the database in limited size. With this technique, even one typical chest CT image set gives an adequate sample size for statistical analysis for it contains hundreds of thousands of image voxels that delineate patient anatomy.

In order to enhance the accuracy of voxel-based analysis, this study established a method to accurately delineate the extent of RILD from CT images and correlate the localization of the injury with radiation dose. Also, most of previous RILD studies used conventional water-based dose algorithms which are not accurate in heterogeneous tissue interfaces [51]. In order to further improve the accuracy of current dose-response models, this study adopted the Monte Carlo method which is currently the most accurate tissue dose calculation model [52]. These methods were retrospectively applied to a group of 5 patients who received 3D-CRT for lung cancer and underwent CT or PET follow-up scans. Time-dependent local dose-response of lung parenchyma was deduced for each individual patient.

Although this study was fully retrospective, it is intended that subsequent investigations which adopt this method would accurately predict the

local dose response, and furthermore provide a clinical evidence that optimization of treatment plan to the individual dose response can improve the outcome of the treatment. To facilitate the future studies with larger population data, this study seek to automate the entire analysis workflow including image registration, injury delineation, and correlation finding. The robustness and uncertainties of a semi-automated process were also investigated.

1.8 Thesis objectives

Under the following hypotheses:

1. Qualitative assessment of RILD can be assisted by semi-automatic image analysis,
2. It is possible to correlate the likelihood of RILD to local radiation dose.

this study is intended to achieve the following objectives:

1. Retrospective patient dose calculation using Monte Carlo method as well as conventional analytical algorithms,
2. Semi-automatic image registration and segmentation of lung and RILD,
3. Investigation of the robustness/uncertainties of a dose-RILD correlation analysis.

1.8.1 Thesis organization

The organization of the thesis is as follows. Image registration is required to conduct a direct comparison of CT images at different acquisition time and setting, and its quality is crucial for accurate quantification of RILD as well as RILD-dose correlation. Thus, chapter 2 will be dedicated to the overview of image registration in theoretical and practical aspects. In chapter 3, detailed description of a tool for this study is described in details. Chapter 4 will present the results of retrospective analysis as well as robustness/precision evaluation of the analysis tool. Discussion on the outcomes and limitations will be offered in Chapter 5. Chapter 6 concludes the text and proposes

the future application of this study. An appendix is provided for details on uncertainty analysis.

CHAPTER 2
Image Registration

2.1 Introduction

In radiation oncology, three-dimensional (3D) medical images of a patient with various modalities (CT, MRI, PET) are acquired for the purposes of diagnosis, treatment planning, follow-up examination, or research. All of these images are stored in a digital format in which the 3D representation of a body is constructed by an array of image intensity elements. One unit of this 3D array is called a voxel. A Cartesian coordinate system (grid) can be defined for each image such that each voxel is assigned of its intensity value and its position with respect to a scanner-dependent reference point. The spatial dimension of a voxel needs to be specified should the voxel-based coordinates be transformed into metric coordinates.

It occurs that two images from different acquisition sessions or different time points within the same session need to be aligned so that corresponding features are spatially related. *Image registration* is the determination of the spatial alignment to achieve the maximum spatial correlation between voxels from the two images. The image to be transformed is the *source image* and the image to be a reference is the *target image*. The maximum spatial correlation is made possible by establishing the accurate correspondence of features between the source and target image. Image registration in its narrow definition simply means the determination of the correspondence. However, registration as a broad concept refers to the whole process of the realization of the correspondence including correspondence determination, coordinate system (grid)

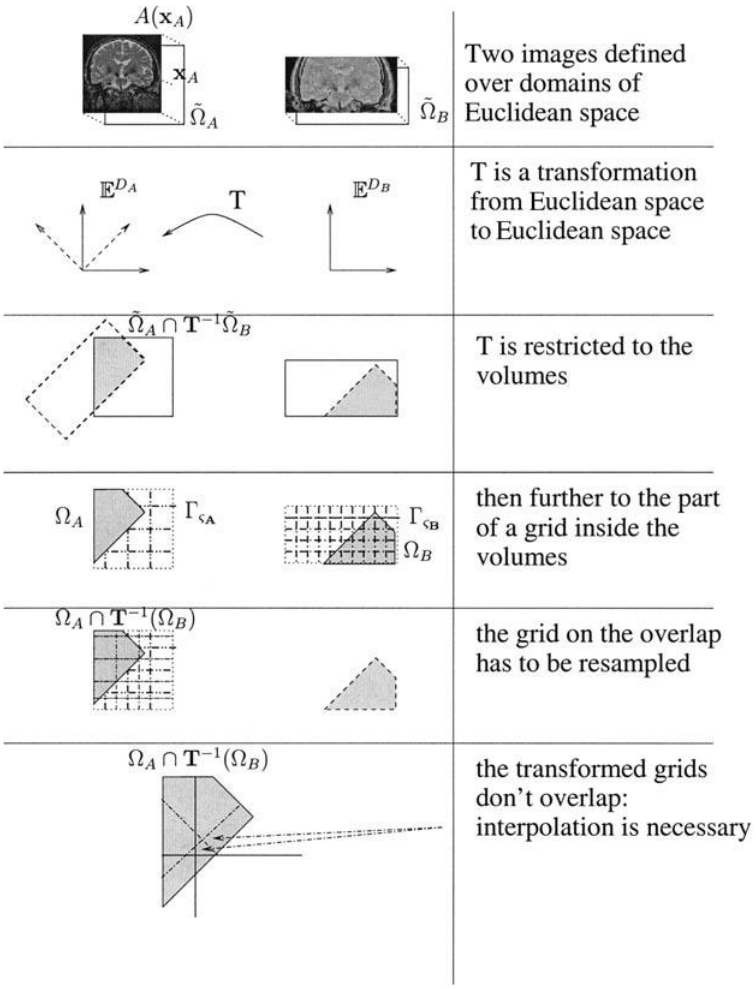

Figure 2.1: Illustration of image resampling and interpolation from [53]: due to the discrete nature of digital images, the transformed image B has to be resampled and interpolated to enable the direct comparison of intensity at the positions of corresponding features. Ω and Γ denotes an image domain and a sampling grid, respectively.

transformation, resampling and interpolation (figure 2.1). Nevertheless, distinction between different registration algorithms lies in the method of determining the correspondence, i.e. the mapping $\mathbf{T}$ that transforms the position x from one image to another:

$$\mathbf{T} : x_s \mapsto x_t \Leftrightarrow T(x_s) = x_t. \tag{2.1}$$

where s and t denote a subset of the source and target image, respectively.

Clinical application of medical image registration is prevalent. As mentioned in Chapter 1, ART requires the re-contouring of targets and organs at risk for daily computed tomograpy (CT) images, which is a demanding task if performed manually. The re-contouring can be fully automated by introducing image registration that can find a grid transformation to propagate manually-drawn contours in a planning CT image onto daily CT images. Image registration is also a necessary tool to combine information from multiple imaging modalities. For example, the extent of a CTV is sometimes not determinable exclusively from anatomical information from CT. Images from functional modalities such as magnetic resonance imaging (MRI) and positron emission tomography (PET) can be aligned with CT through registration to assist the delineation of a biologically relevant target. In neuroscience, the identification of brain structures is facilitated by transforming an individual brain image obtained through MRI or PET into a patient-independent standard reference frame called Taliarach coordinate system [54].

2.2 Classification

A number of classifications of image registration models were made by van den Elsen et al. [55] and Maintz and Viergever [56] according to its dimensionality, nature of transformation, domain of transformation, optimization procedures, modality involved, and et cetera. The most widely accepted classification in the literature makes a division based on the nature of flexibility : linear versus deformable (also called non-linear) registration. They fundamentally differ in that the former finds a single global solution while in the latter there can be a number of locally defined solutions.

2.2.1 Linear registration

Linear registration models the transformation of space as the combination of translation, rotation, scaling, and shearing. Linear registration can be either

rigid or affine, depending on how many of these transformation modes are used. Rigid registration is subject to rigid body constraints: image frames are only allowed to rotate and/or translate. Affine registration is carried out with every possible mode. While the rigid transformation preserves the distance between two points, the affine transformation preserves parallel lines.

Linear transformation enables the mapping of a point $(x, y, z, 1)$ [1] in a source image to the point $(x', y', z', 1)$ in the reference frame of a target by a simple multiplication by a 4 X 4 transformation matrix **A**:

$$(x', y', z', 1) = [\mathbf{A}](x, y, z, 1)'. \tag{2.2}$$

In the case of the affine transformation, the matrix **A** contains 12 independent parameters which are determined by a computation process. The matrix **A** can be factorized into 4 matrices, representing translation, rotation, scaling and shear:

$$\mathbf{A} = [\mathbf{Sh}][\mathbf{Sc}][\mathbf{R}][\mathbf{T}]. \tag{2.3}$$

The matrices T, R, Sc, Sh are defined as follows:

$$\mathbf{T} = \begin{bmatrix} 1 & 0 & 0 & tx \\ 0 & 1 & 0 & ty \\ 0 & 0 & 1 & tz \\ 0 & 0 & 0 & 1 \end{bmatrix} \tag{2.4}$$

[1] the fourth coordinate, 1, is a pseudo-coordinate to enable translation through matrix multiplication.

where tx, ty, and tz are the translations in x, y, and z between the two points.

$$\mathbf{R} = [\mathbf{\Theta}][\mathbf{\Phi}][\mathbf{\Psi}] \tag{2.5}$$

where

$$\mathbf{\Theta} = \begin{bmatrix} 1 & 0 & 0 & 0 \\ 0 & cos\theta & sin\theta & 0 \\ 0 & -sin\theta & cos\theta & 0 \\ 0 & 0 & 0 & 1 \end{bmatrix} \tag{2.6}$$

$$\mathbf{\Phi} = \begin{bmatrix} cos\phi & 0 & -sin\phi & 0 \\ 0 & 1 & 0 & 0 \\ sin\phi & 0 & cos\phi & 0 \\ 0 & 0 & 0 & 1 \end{bmatrix} \tag{2.7}$$

$$\mathbf{\Psi} = \begin{bmatrix} cos\psi & sin\psi & 0 & 0 \\ -sin\psi & cos\psi & 0 & 0 \\ 0 & 0 & 1 & 0 \\ 0 & 0 & 0 & 1 \end{bmatrix} \tag{2.8}$$

and the angles θ, ϕ and ψ are clockwise rotations around the $x-$, $y-$, and $z-$ axes, respectively. The scaling matrix $\mathbf{S}$ is defined by:

$$\mathbf{Sc} = \begin{bmatrix} sx & 0 & 0 & 0 \\ 0 & sy & 0 & 0 \\ 0 & 0 & sz & 0 \\ 0 & 0 & 0 & 1 \end{bmatrix} \tag{2.9}$$

where sx, sy, and sz are scaling factors along each of the axes.

$$\mathbf{Sh} = \begin{bmatrix} 1 & 0 & 0 & 0 \\ a & 1 & 0 & 0 \\ b & c & 1 & 0 \\ 0 & 0 & 0 & 1 \end{bmatrix} \tag{2.10}$$

where a, b, and c are the three skewing parameters designated to the shearing of a rectangular parallelpiped into an oblique one. When all the scaling factors are unity and all the skewing parameters are zero, the affine transformation is reduced to the rigid transformation.

The number of parameters, or the number of transformation modes, depends on the properties of an object to be registered. Intra-subject registration of brain or skeleton, for example, can be done by rigid transformation because it is adequate to assume that brains or bones do not change their size or shape over time. More parameters will be needed to account for more complex morphometric changes. Affine registration is useful in correcting for calibration difference between scanners or the alignment of brain images from different subjects [57].

2.2.2 Deformable registration

The major limitation in linear registration is that transformation cannot be locally varied. As a result, matching of features in one region might be achieved at a cost of mismatching in another region. Such problem arises for images that are affected by the change in posture, breathing phase, or bladder/stomach contents. In response to this issue, deformable registration was developed to permit local matching following the preliminary global alignment (Figure 2.2). Due to the regional variation in the deformation, transformation cannot be modeled as a matrix multiplication process. Instead, a deformation vector field (DVF), defined on an isotropic 3D cubic lattice in the domain of

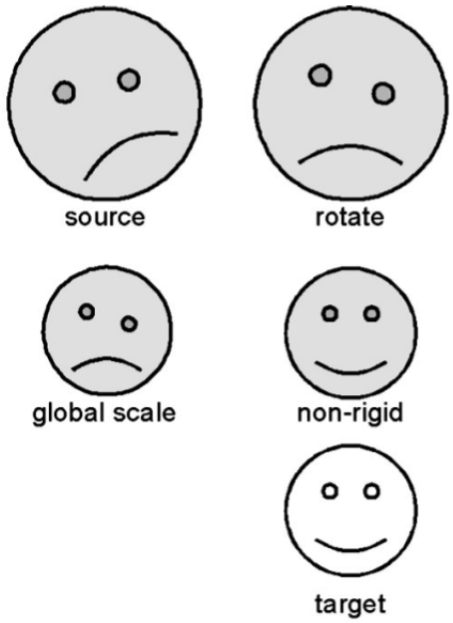

Figure 2.2: Illustration showing the improvement of similarity by nonlinear registration. The differences in internal structures not dealt by rotation and scaling can be corrected by a series of additional steps. Reproduced from [58]

a source image, dictates how an individual voxel in the source image will be translated to match a target image. The necessity for local adaptation dramatically increases the degree of freedom that the transformation should allow, which makes computation much more demanding compared to the linear registration. A transformation model that assigns proper boundary conditions is established to help the registration find a realistic solution as well as to reduce the computational demand. According to the model to be used, nonlinear registration can be further categorized into spline-based registration and physical-model-based registration.

Spline-based registration: A spline is a group of 2-dimensional piecewise polynomials which can be geometrically seen as a "plate", serving as a basis function for an arbitrary 2D function. A spline-based registration algorithm requires corresponding ("control") points in the source and target image. The

displacement between the control points determines the optimal linear combination of splines. The splines are interpolated to define correspondences away from these points. Too much bending of the splines is restricted by increasing the value of a cost function during optimization. The control points can be fiducial markers, user-defined, or automatically extracted region corners using a shift-invariant feature transform (SIFT) algorithm [59]. There are two types of commonly used splines: thin-plate splines and B-splines. Thin-plate spline has a global influence and this it is applicable to linear affine registration [60]. Due to the lack of local flexibility, however, computational cost rises steeply as more control points are added. As an alternative, B-splines are only defined in the vicinity of each control point and known to be quicker and more flexible than thin-plate splines [58].

Physical model-based registration: For deformable registration based on physical models, the source image can be modeled as a moving scene (optical), an elastic (elastic registration) or a diffusive material (demons). Local deformation is determined such that it obeys the kinetic law (e.g. Hooke's law) of the particular model. Physical model-based registration is non-parametric and thus more flexible than spline-based registration, but the estimation of realistic correspondence is the biggest challenge [61]. Thus, every algorithm using physical models maximizes an objective function by minimizing a cost function that regulates large deformation as well as maximizing an image similarity function. *Optical flow,* originally proposed by Horn and Schunck [62], calculates the movement of bright objects in a source image from a source to a target image under the condition that the overall brightness of an image is constant. The obtained velocity field is deemed equivalent to a deformation field. An additional constraint on the smoothness of a velocity field is imposed. *Demon's algorithm* proposed by Thirion [63] models the image registration as

Name	Type	Smoothness constraints	Characteristics	References
rigid	linear	none	preserves distances	[65], [66]
affine	linear	none	preserves parallel lines	[54], [67]
thin-plate splines	linear/nonlinear	spline bending	global influence	[68], [69]
B-splines	nonlinear	spline bending	local influence	[70],[71]
Optical flow	nonlinear	gradient of velocity field	constant brightness assumption	[62],[72]
Demon	nonlinear	gradient of velocity field		[63],[73]
Elastic	nonlinear	linear-elastic	small deformation assumption	[64], [74]

Table 2.1: Comparison of registration models in section 2.2.

a diffusion process. The source image is allowed to diffuse onto the target image until the two images are aligned. Points in the target image, acting as "demons", attracts the points in the source image which are similar. Each iteration in optimization processes calculates the force of attraction which is applied to update a velocity field. In *elastic registration* [64], a source image is modeled as an elastic solid deformed by forces derived from image similarity measures. The image is deformed until an equilibrium between similarity-driven forces and elastic forces is achieved. However, due to its computation complexity and small deformation assumption that the equilibrium condition requires, the application of elastic registration to clinical settings is limited.

See the table 2.1 for the summary registration models and useful references.

2.3 Similarity metrics

In general, transformation is determined in an iterative fashion: the measure of similarity, or similarity metrics, is calculated for each iteration and the transformation is recursively updated to improve the similarity scoring. For linear registration, image similarity can be an used as an objective function for optimization. For deformable registration, however, a similarity condition alone is not enough to find a unique optimal solution in the increased dimensions of transformation parameter space. To ensure the uniqueness of the solution, smoothness constraints are added to form an objective function, often called a system energy functional, which is a weighted sum of the similarity metric and a cost function derived from the smoothness constraints. There are three different approaches of measuring the similarity between two images: it can be calculated directly from voxel values in the images (voxel-based) or from geometrical structures such as landmarks or surfaces derived from the images (geometry-based). Alternatively, joint probability distribution of intensity occurrence can be constructed to derive statistical dependency between the images (statistics-based).

2.3.1 Voxel-based metrics

Sum of squared intensity difference (SSID): SSID is one of the simplest representation of image similarity under the assumption that the intensity of two images are different only by random noise. For N voxels in the domain of overlap between images $\mathbf{A}$ and $\mathbf{B}$ ($\Omega^{\mathbf{T}}_{\mathbf{A},\mathbf{B}}$),

$$SSID = \frac{1}{N} \sum_{x \in \Omega^{\mathbf{T}}_{\mathbf{A},\mathbf{B}}} |\mathbf{A}(x) - \mathbf{B}^{\mathbf{T}}(x)|^2 \tag{2.11}$$

Its main advantage is simplicity, which makes it suited for fast optimization. The SSID is not applicable to inter-modality registration because pixel values are systematically different. Also, the existence of a small number of

voxels with large intensity differences may bias the SSID value. Thus, it is not robust when image artifacts are present.

Cross-correlation (CC): Correlation technique assumes a linear relationship between grey values in the images. A normalized CC coefficient is defined as:

$$CC = \frac{\sum_{x \in \Omega^{\mathbf{T}}_{\mathbf{A},\mathbf{B}}} (\mathbf{A}(x) - \bar{\mathbf{A}})(\mathbf{B}^{\mathbf{T}}(x) - \bar{\mathbf{B}})}{\{\sum_{x \in \Omega^{\mathbf{T}}_{\mathbf{A},\mathbf{B}}} (\mathbf{A}(x) - \bar{\mathbf{A}})^2 \sum_{x \in \Omega^{\mathbf{T}}_{\mathbf{A},\mathbf{B}}} (\mathbf{B}^{\mathbf{T}}(x) - \bar{\mathbf{B}})^2\}^{1/2}} \tag{2.12}$$

where $\bar{\mathbf{A}}$ and $\bar{\mathbf{B}}$ is the mean voxel value in image $\mathbf{A}$ and $\mathbf{B}^{\mathbf{T}}$, respectively. It can be used for either intra- or inter-modality registration. As for SSID, CC is sensitive to the presence of "outlier" objects such as patient table, surgical instruments, and etc. This limitation can be overcome by manually removing those outliers from the image or weighting pixel values in the coefficient to explicitly handle the outliers [75].

2.3.2 Geometry-based metrics

Specific geometric features such as points or surfaces can be extracted from images either automatically or interactively, and the average displacement between homologous points, curves or surfaces can be used as a similarity metric. Point-based and surface-based registration is driven by the geometry-based metrics. Point-based registration seeks the transformation that forces the corresponding points to be aligned in a least-square sense. An optimal solution $\mathbf{T}$ of this problem (also known as Procrustes problem) minimizes a cost function $G(\mathbf{T}) = (\sum_i |\mathbf{T}(p_i) - q_i|^2)^{\frac{1}{2}}$ for given control points p_i and q_i in a source and a target image, respectively. This concept can be extended to 1D (e.g., crests or fissures) or 2D (e.g., ventricular walls) feature matching where the curves or surfaces are modeled as densely populated points [76]. Biological validity of transformation can be ensured by using specific anatomical structures as control features as long as the identification of those features is carried out by experienced personnel.

2.3.3 Statistics-based metrics

When two images are not from the same modality, direct comparison of voxel values is not applicable. Instead, statistical dependency between the images can be maximized using the concept of *information*. When two images are best aligned, the amount of shared information is maximized while that of the combined image is minimized. The most commonly used measure of information is the Shannon-Wiener definition of entropy H [77]:

$$H = -\sum_{i} p_i \log p_i \tag{2.13}$$

H is the average information supplied by a set of i symbols whose probabilities are given by p_i. H is maximal when all symbols are equally probable, and a minimum when only one symbol is occurring. When this formulation is applied to a medical image, p_i can be interpreted as a discrete variable $p_A(a)$ which is the probability of occurrence of a given voxel intensity a within image A. When two images are brought together, an entropy of a combined image (joint entropy) can be expressed in a similar fashion:

$$H(A, B) = -\sum_{b \in \mathbf{B}} \sum_{a \in \mathbf{A}} p_{\mathbf{AB}}(a, b) \log p_{\mathbf{AB}}(a, b) \tag{2.14}$$

where $p_{AB}(a, b)$, named as a joint probability density function (PDF), is the probability of the joint occurrence of a given voxel intensity a in image A with an intensity b in image B. If A and B are totally unrelated, then the join entropy will be the sum of the entropies of the individual images. The better aligned the two images are, the lower the joint entropy compared with the sum of the individual entropies:

$$H(\mathbf{A}, \mathbf{B}) \leq H(\mathbf{A}) + H(\mathbf{B}) \tag{2.15}$$

Although joint entropy alone can be used as a similar metric, it can be biased by the presence of nonoverlapping regions [78]. The solution is to consider only the region where the two images overlap. Collignon [79] and Viola [80] introduced the concept of mutual information $I(A, B)$ which is the entropy of the joint system excluding marginal entropies. The definition of $I(A, b)$ is the following:

$$I(\mathbf{A}, \mathbf{B}) = H(\mathbf{A}) + H(\mathbf{B}) - H(\mathbf{A}, \mathbf{B}) = \sum_{b \in \mathbf{B}} \sum_{a \in \mathbf{A}} p_{\mathbf{AB}} log \frac{p_{AB}(a, b)}{p_A(a) p_B(b)} \quad (2.16)$$

The problem of registration is now to find the transformation that maximizes mutual information by minimizing the information in the combined image (joint entropy). However, I(A,B) is a function of how much information is provided in the overlap as well as how well the two images align. To overcome the dependency on the amount of overlap, mutual information can be normalized to the joint entropy of the overlapping region:

$$NMI(\mathbf{A}, \mathbf{B}) = \frac{I(\mathbf{A}, \mathbf{B})}{H(\mathbf{A}, \mathbf{B})} \quad (2.17)$$

Mutual information is extremely useful for inter-modality registration and found to be more robust and precise than cross correlation or joint entropy for MR-CT and MR-PET brain image registration [66] [81]. For intra-modality image registration, however, the robustness depends on the particular images being registered [75].

2.4 Optimization method

The problem of finding the best transformation is reduced to searching for the global optimum of a similarity function or, if a constraint is included, a system energy function. As mentioned, the optimum is found by gradually tuning the transformation by trial and error. Practical difficulties of this

method is associated with the high-dimensionality of the space that objective function lies in (for example, $\Re^{12}$ for affine registration) and the fact that there are multiple local optima besides a global optimum. Searching the entire parameter space for a global optimum is computationally demanding as the complexity of a transformation model increases, because required computation increases with a power of the degrees of freedom. Therefore, it is practical to start the registration with a reasonable initial estimate and find the nearest optimum from the initial estimate. However, it is very likely that optimization converges to an incorrect solution called a "local optimum" if the starting estimate is incorrect.

A multi-resolution or coarse-to-fine approach is a widely accepted strategy for either linear or deformable registration to cope with the problems of computational cost and local optimum. In this approach, registration is hierarchically sequenced in a way that the transformation found in a coarse resolution step is used as initial transformation for a finer resolution step. Prior to the registration for each resolution step, source and target images are blurred thereby smoothing an objective function in a parameter space, which removes small local optima. The blurring of images can also be understood as filtering the images to extract features in a desired scale. The largest resolution step aligns the gross features, and smaller details are added on to refine the fit as the registration descends the hierarchy. Feature detection by blurring is implemented by convolution with 3D isotropic Gaussian kernels. The convolution operation is shift and rotationally invariant: in other words, the feature detected at a particular point will be identical even if the image is rotated or translated [82].

However, the multiresolution approach does not entirely guarantee the best transformation to be found. First of all, due to the limitation of similarity metrics on reflecting physical similarity, the global optimum of an optimization function may not correspond to a desired solution. Also, the initial transformation of the most coarse image has to be arbitrarily determined. This can be done by manual alignment and/or principle axis transformation (PAT) where two images, modeled as rigid bodies, are rotated and translated until their centers of mass and principal axes are aligned [83]. The success of this approach heavily depends on the faithfulness of the starting estimate.

2.5 Validation of registration

The accuracy of the registration can be verified quantitatively or qualitatively. The registered image can be qualitatively compared to the target image by visual inspection. Quantification of the accuracy of registration is a challenging task, because the ground truth is usually not provided for patient images. Also, image matching may vary in regions, so representing the accuracy by one average error value can be misleading.

2.5.1 Landmark-based validation

Registration can be verified based on how well it can aligns certain features as it is predicted. The average displacement between corresponding landmarks can be a measure of accuracy. Readily identifiable anatomical features such as blood vessels or bronchial bifurcation can be used as the landmarks. Since this is a fully manual process, the error in landmark identification has to determined from inter-observer variability.

2.5.2 Similarity metrics

Similarity scores as described in section 2.3 can be used to quantify registration error. These metrics are easily available as they can be tracked during optimization process. However, similarity metrics assess only global matching

and thus no information on local mismatch is available. A potential solution is to evaluate the metrics within a user-defined region of interest.

2.5.3 Contour matching

In radiotherapy, automatic recontouring is an important application of deformable image registration. Manually drawn contours can serve as a ground truth by which to evaluate the performance of image registration. The agreement between the manually drawn and deformed contours can be represented by: i) distance-to-agreement (DTA), and ii) Dice's coefficient. The DTA between two contours can be obtained by taking radial projection from the center of mass of one of the contours or drawing a line normal to the surface of one contour. If an average DTA is sought, Dice's coefficients in statistics is a measure of the agreement of two sets A and B:

$$s = \frac{2|A \cap B|}{|A + B|} \tag{2.18}$$

A Dice's coefficient ranges from 0 to 1, where two identical contours have a value of 1.

CHAPTER 3
Materials and Methods

3.1 Overview

Through the methods described in this chapter, patient information was retrieved from archives, processed, and analyzed to deduce the spatial correlation between RILD and radiation dose. Patient data are fed into two independent software tools which implement image processing and dose calculation to obtain injury (RILD) and dose distribution, respectively. The image was processed into three sequential steps: i) image registration, ii) image intensity calibration, and iii) segmentation of lung and injury. A flowchart shown in 3.1 illustrates the overview of the workflow:

3.2 Subjects

Five non-small-cell lung cancer (NSCLC) patients, admitted to the Montreal General Hospital (MGH) between 2006 and 2007, were selected as the subjects for this study. They were 4 males and 1 female with a median age of 60. They all received 3D-CRT under conventional fractionation (60 Gy in 30

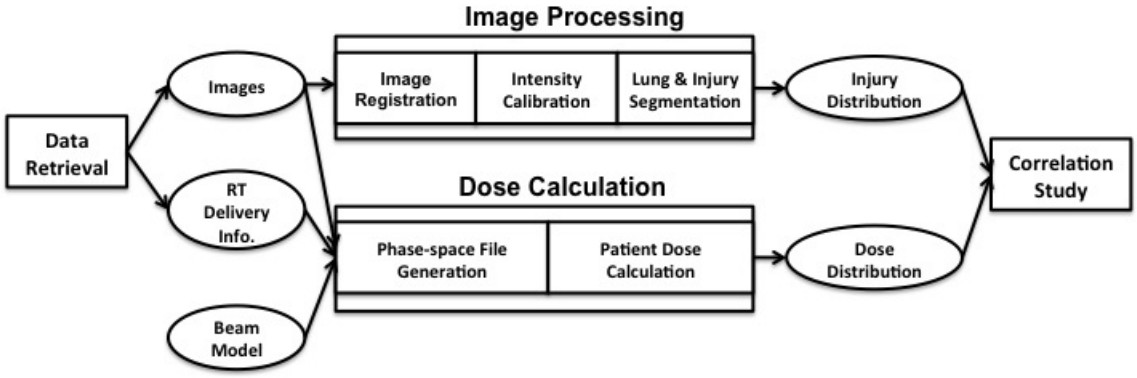

Figure 3.1: Block diagram illustrating the workflow of the analysis.

Number	Age	Sex (M/F)	Tumor stage	Chemotherapy	Respiratory symptoms(O/X)
1	75	M	T3N3M0	neoadjuvant + concomitant	O
2	65	M	T4N3M0	neoadjuvant	X
3	51	M	T1N3M0	neoadjuvant + concomitant	X
4	60	M	T1N3M0	none	O
5	49	F	T3N3M0	concomitant	X

Table 3.1: Survey on 5 subjects observed for this study.

fractions over 6 weeks) while chemotherapy regimes were not controlled (Table 3.1). 2 Patients developed respiratory symptoms (increasing cough and dyspnea) within one month after the completion of the treatment and were prescribed with cortisone (patient 1) or prednisone (patient 2) to mitigate the symptoms.

3.3 Patient data

3.3.1 Images

The patients underwent a CT simulation scan prior to RT and follow-up diagnostic scans after the RT. The simulation (planning) CT images were obtained with flat tabletop scanners. The patients were allowed to breathe freely in a supine and overhead arm positions. The follow-up (post-RT) studies comprise chest CT and whole-body PET/CT scans, all using curved tabletop scanners with normal arm positioning. Prior to every PET scan, a CT scan for attenuation correction was acquired with identical body position. For every follow-up CT scans, the patients were at breath-hold during the acquisition which took 3 seconds. The time intervals for the post-RT scans were not regular as long-term observation was subject to patient health or death. Every image was stored under Digital Imaging and Communication in Medicine (DICOM) standards. The post-RT images were retrieved from the

Picture Archiving and Communication System (PACS) at the MGH whereas the planning CT images were exported from the treatment planning system.

3.3.2 Treatment plans

Patient Treatment plans which were electronically created on Eclipse^{TM}(Varian Medical Systems, Palo Alto, CA) treatment planning system (TPS) were retrieved from Varian Oncology Information System (ARIA). Treatment planning information for each patient includes: i) an electronic radio-oncology chart summarizing disease status and RT/ChT prescription, ii) a planning CT image set and associated contours for CTV, PTV, body, and notable organs, and iii) external beam delivery information which included beam geometry defined on the planning CT, accessories such as MLC and wedge, and the number of monitor units (MUs) for each beam.

3.4 Beam models

Patient dose calculation using Monte Carlo Method requires an accelerator or a beam model which is a virtual representation of radiotherapy sources. The Varian Clinac 21X linear accelerator in the MGH was used for every treatments and its Monte-Carlo model was built for two energy beams (6 MV, 18 MV). Details on the description of beam models and its construction and verification will be described in the section 3.8.2.

3.5 Image registration

In order to enable voxel-wise density comparison, follow-up CT and PET images were registered to a planning CT image which served as a reference image.

3.5.1 Registration software

The Automatic Non-Linear Image Matching and Anatomical Labeling (ANIMAL) toolkits [84], developed at the Montreal Neurological Institute by Dr. D. L. Collins, were chosen for registration software. The ANIMAL

not only provides different options for registration algorithms (affine or deformable) but also allows for pre-registration image manipulation such as offset, blurring and intensity gradient magnitude.

3.5.2 Choice of registration algorithm

Due to the absence of local correspondence, deformable registration is naturally biased by the asymmetric presence of hyperintensities such as fibrosis in lung or multiple sclerosis in brain. Most authors prefer to use affine registration in the presence of those lesions [85] [86]. To preserve anatomical changes (RILD occurrence and tumor shrinkage), 12-parameter affine registration was chosen over deformable registration despite its lack of flexibility to reproduce lung deformation. Multi-resolutional approach was used to save computation time and avoid the local minima of an objective function. Cross-correlation (CC) was selected as an objective function to drive the optimization process. Since CC assumes a linear relationship between intensities, the difference in intensity calibration between diagnostic CT and planning CT was not expected to bias the registration.

3.5.3 Pre-registration steps

The format of the retrieved images was converted from the DICOM to the Medical Identification Number for Canada (MINC) format which is a required input format for the ANIMAL. In the MINC format, images are given their physical dimension by specifying the size of a voxel in x-, y-, and z-directions. The converted CT images are given the offset of 1000 to prevent any negative intensity in the region to be aligned. The CT image sets with the offset were blurred prior to registration by convolving 16 mm, 8 mm, 4 mm, and 2 mm full-with-half-maximum (FWHM) 3D Gaussian kernels. Binary lung masks for each CT images were generated by segmenting the intensities within the

HU range [50,800] followed by removal of airways and primary bronchi (Figure 3.2).

3.5.4 Transformation optimization

The best estimate of the transformation of a source (follow-up) to resemble a target (planning) CT image was obtained through an iterative optimization process. Registration began with rough alignment of the images by shifting the center of mass (COM) of the mask volume of the source to the corresponding location of the target. The resulting transformation was used as an initial transformation for the registration for the largest resolution step (16 mm). The optimized transformation for each resolution step was passed onto its subsequent step in the same manner. The resulting transformation for the smallest (4 mm) resolution step was used as a final estimate because no significant improvement in image similarity evaluated by CC was observed beyond 4 mm resolution step (figure 3.3).

The optimization for each resolution step yielded the transformation that maximizes the value of CC in a given scale. CC was evaluated on the nodes of a 3D lattice defined on the smallest of two lung mask volumes. In this way, the coordinates of the lattice were used to specify positions in one volume, and when mapped through the transformation matrix, specify homologous positions in the other volume. The spacing between lattice nodes was always set to be 0.5 x FWHM of Gaussian blurring kernels so that image sampling frequency was enough to satisfy the Nyquist's condition to prevent aliasing. The global maximum of the CC in a given resolution was searched using a simplex algorithm. A radius of 20 mm was used for the simplex volume during the coarsest registration step and was reduced to 10 mm for the following steps.

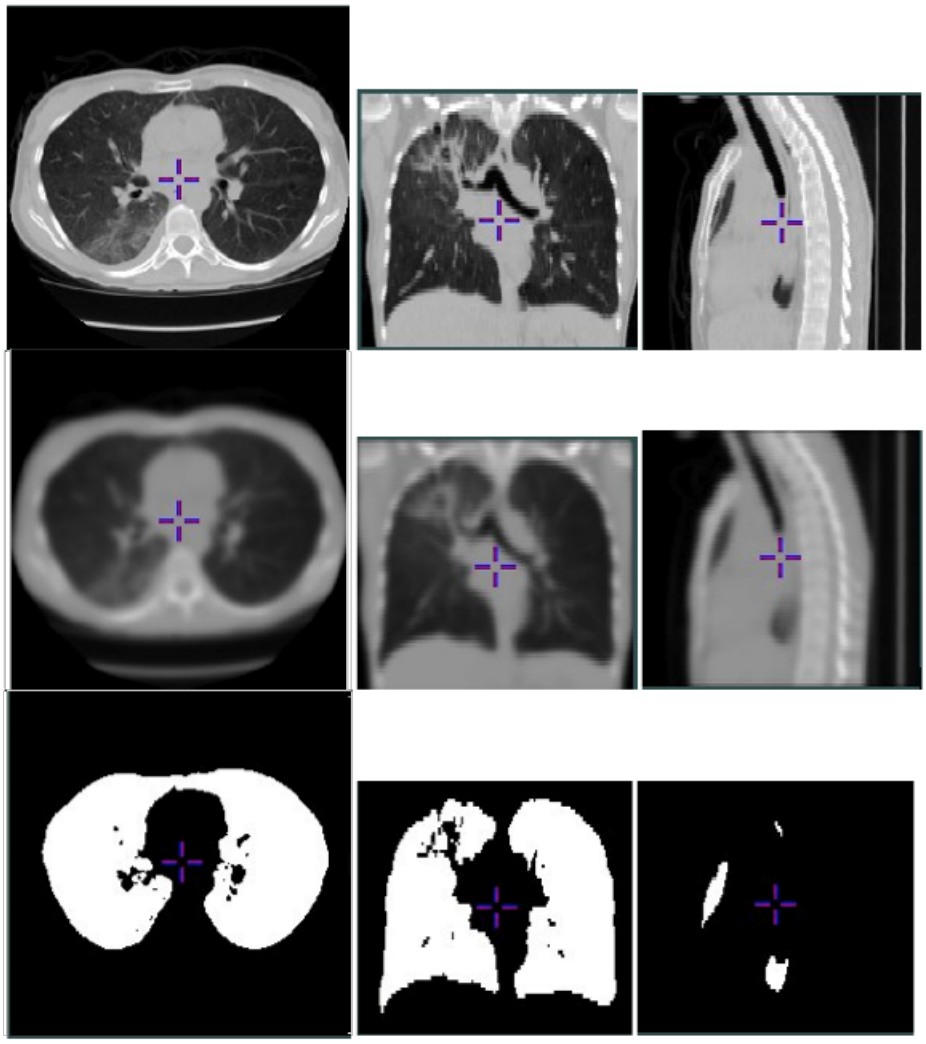

Figure 3.2: Pre-registration image processing. First row: axial (left), coronal (middle) and sagittal (right) slices through the original chest CT image, second row: the same slices blurred with a 8 mm FWHM Gaussian kernel, third row: the corresponding slices of a binary lung mask with 1 and null shown in white and black respectively.

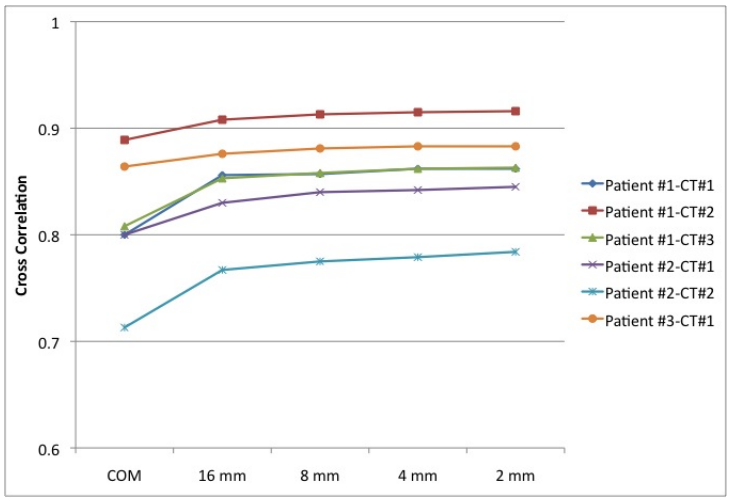

Figure 3.3: Change in image similarity in terms of cross correlation during multi-resolutional optimization. The cross correlation was evaluated at 2 mm grid between a target and the source transformed using 5 intermediate optimization results : alignment of center of mass (COM) and four resolution steps (16 mm, 8 mm, 4 mm, and 2 mm).

3.5.5 Post-registration processing

The optimized transformation function, saved as a 4×4 matrix format, was used to redefine an image coordinate in which new voxel values were determined using trilinear interpolation. The image domain and grid size of the new image coordinate was set to match those of the reference image (planning CT). Post-RT PET images were also resampled to the grid of the reference image using the transformation optimized for the CT image from the same scanning session.

3.5.6 Verification

The accuracy of registration was evaluated both qualitatively and quantitatively. Initially, the matching of lung contours and pulmonary arteries was carefully inspected. If the visual agreement was deemed acceptable, left and right lungs were contoured separately from segmented lung volumes (segmentation procedures to be described later). The contours were superimposed onto the corresponding contours from the planning CT image (figure 3.4), and

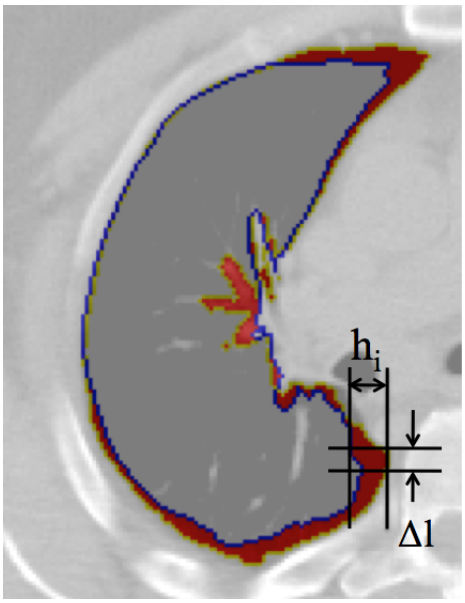

Figure 3.4: Measurement of in-slice DTA which evaluates the average displacement between planning CT (yellow) and post-RT (blue) lung contours. Red patches, defined as regions surrounded by only one contour, represent the area of contour mismatch.

the area of the regions that are surrounded by only one contour was found. In-slice distance-to-agreement (DTA) between the contours was calculated as the ratio of the area to the contour length from the planning CT [1] . The average of in-slice DTA over the slice range where injury was scored was calculated as the global DTA.

[1] The area of red regions in figure 3.4 at slice k, A_k, can be approximated as a sum of N_k finite areas:

$$A_k = \Delta l \sum_{i=1}^{N_k} h_i = N_k \Delta l \bar{h}_k \sim L_k \bar{h}_k \tag{3.1}$$

where $\bar{h}_k = \frac{1}{N_k} \sum_{i=1} N_k h_i$ is the average displacement between the contours at slice k, and L_k is the contour length from the planning CT. Thus, the expression for the in-slice DTA is: $DTA_k = \bar{h_k} = A_k / L_k$

3.6 Intensity calibration

3.6.1 CT calibration

CT imaging measures the spatial distribution of photon attenuation coefficients (μ) expressed in Hounsfield Units (HU) which is defined as follows:

$$HU = \frac{\mu - \mu_w}{\mu_w} \tag{3.2}$$

where μ_w is the attenuation coefficient of water.

The attenuation coefficient is associated with physical density ρ via the following relationship:

$$\mu = \tau + \sigma_R + \sigma_C + \kappa = \rho N_A \frac{Z}{A}({}_e\tau + {}_e\,\sigma_R + {}_e\,\sigma_C) \tag{3.3}$$

where N_A is the Avogadro number, $\frac{Z}{A}$ is effective atomic number to mass ratio, and τ, σ_C, σ_R are the cross-sections for photoelectric effect, Compton scattering and Rayleigh scattering, respectively (the left subscript e is used for electronic cross-sections). Since Compton scattering is the dominating photon interaction in tissue in diagnostic energy range, the μ can be simplified as:

$$\mu \sim \rho N_A \frac{Z}{A} {}_e\sigma_C \tag{3.4}$$

The proportionality between μ and ρ is derived from the approximate independency of the values of Z/A and ${}_e\sigma_C$ on the type of materials.

Phantoms containing tissue-equivalent plugs are often used for empirical determination of the HU-ρ relationship. Measured HUs for materials with known density values can be fitted with a double straight line approach [87]. Due to the retrospective nature of this study, however, calibration functions for the scanners at the time of the scan were not available. Instead, CT images were retrospectively calibrated based on measured HUs in the image itself. In

order to account for scanner specificity, one calibration function was assigned to one scanner type. The calibration function for each scanner was found by the following three-step processes:

Relative (cross) calibration: Difference in calibration between scanners were corrected by the affine scaling of the HUs of the post-RT CT images to those of a reference image (planning CT). The average HUs for 13 sites in thorax and abdomen were taken from each CT image set. A volume of interest (VOI) was chosen for each site by marking a region with an area $0.3 \sim 0.6cm^2$ over 5 slices to minimize a partial volume averaging artifact[2] . A scatter plot of the 13 sampled HUs from one diagnostic CT image against the reference CT image was drawn, and a line was least-square fit to the plot. The best-fit line was applied to renormalize the pixel values of the post-RT CT images.

Absolute calibration: The pixel values of the reference image were converted to physical density in a similar fashion. The 13 sites sampled from above were grouped into 8 organs or tissues (liver, kidney, spleen, muscle, fat, vertebral body, trachea (air), spinal cord) and an average HU was determined for each category. The HUs were plotted against physical density values derived from the ICRP reference man [88]. On the plot, two linear functions crossing at HU = 50 were determined by a least-square fit (Figure 3.5). The resulting function, represented by four regression parameters (2 slopes and 2 intercepts) was used to convert the HUs of the planning or renormalized diagnostic CT images to physical density.

[2] Partial volume averaging occurs when there is more than one structure within a pixel or voxel. The resulting voxel value is the area- or volume-weighted average of adjoining structures.

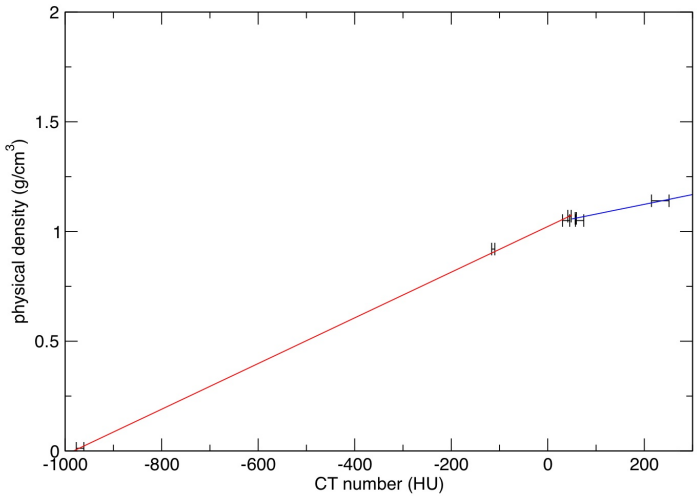

Figure 3.5: Conversion of planning CT numbers to physical density. Regression was performed separately in two ranges for $HU > 50$ (red) and for $HU < 50$ (blue).

Determination of scanner-specific CT calibration: There were 6 scanner models identified from the patient database (table 3.2). For each scanner model, a pool of the values of the four regression parameters was generated from 5 patients. The average values of the parameters within the pool were taken as calibration parameters to be used for that scanner (Figure 3.6). The standard deviation of the mean value of the parameters within the pool was small compared to the combined fitting uncertainty ($p < 0.01$).

3.7 Lung and injury segmentation

3.7.1 Lung segmentation

Lung segmentation was created for each of planning and registered post-RT CT images. The initial lung segmentation was 8created by applying a threshold of HU: [-1000,-300]. Then, 3D connectivity analysis [3] identified an isolated volume of 2000∼5000 ml from the initial segmentation, which removed

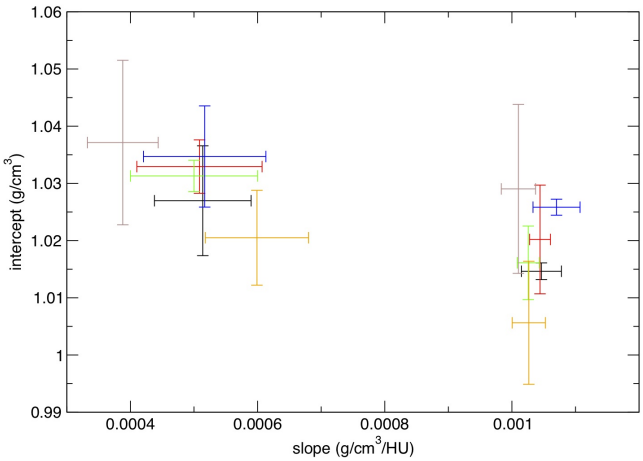

Figure 3.6: Scatter plot of the two slopes (x-axis) and corresponding intercepts (y-axis) of the CT calibration functions for 6 scanners (scanner 1:black, scanner 2: red, scanner 3: green, scanner 4: blue, scanner 5: orange, scanner 6: brown).

Number	Model name	Type	kVp
1	GE lightspeed VCT	diagnostic CT	120
2	GE discovery ST	diagnostic PET/CT	140
3	Philips AcQSim	planning CT	120
4	GE lightspeed QX/i	diagnostic CT	120
5	GE HiSpeed CT	diagnostic CT	120
6	Toshiba Acquilion	diagnostic CT	120

Table 3.2: 6 scanner models as identified from DICOM headers.

non-lung voxels such as the space outside the body, stomach or bowels. Airways and primary bronchus, not classified as yet appended to lung, had to be manually removed. Additional manual correction was applied to fill in the interiors of lung. PTV volume was removed from lung segmentation due to the impossibility to differentiate residual and recurrent tumor from RILD. The resulting lung segmentation was automatically separated into left and right lung by slice-by-slice 2D connectivity analysis.

3.7.2 Injury segmentation

Local density change ($\delta\rho$) over a period of a given post-RT time was evaluated at each voxel position by subtracting the calibrated density value of the planning CT from the post-RT CT. RILD volume was segmented on the $\delta\rho$ image as the voxels showing the pathological level of physical density change. The upper and lower limits of such change, as of clinical studies by Rosen et al. [15], were determined as 2 times standard deviation of the distribution of regional lung density change for CT-examined symptomatic (RILD or RTOG/ETORC grade 2 or higher) patients. The segmentation was performed within post-RT lung segmentation to rule out the voxels showing density change due to contour mismatching.

3.8 Dose calculation

3D dose distribution in patient thorax was retrospectively calculated using a calculation model and retrieved treatment plans that were actually delivered to the patients. Two calculation models were used: the Varian Anisotropic Analytical Algorithm (AAA) and the EGSnrc-based Monte-Carlo (MC) simulation.

[3] 26-connectivity was used where two voxels are regarded to be connected if they share at least one point, side and face.

3.8.1 Calculation by AAA

The analytical anisotropic algorithm (AAA) has been implemented in the Eclipse^{TM}TPS to enhance the accuracy of its previous generation (pencil beam convolution) in heterogeneous media while maintaining reasonable computation time (around a few seconds per beam) which is a comparative advantage over MC. The implementation of the AAA algorithm consists of two parts: the configuration module characterizes a beam from a linear accelerator by optimizing a number of parameters by means of minimizing the discrepancy from measured beam data. The second part, dose calculation module, models dose deposition as the superposition of dose components from primary photons, secondary photons, and electron contamination. The dose from photons is calculated as a convolution of scatter kernels which are 3D exponential functions representing the interaction of the photon beam in a dose voxel [89]. The magnitude of the kernels is scaled according to the electron density of a voxel, which enables heterogeneity correction.

The accuracy of the algorithm, with its testing schemes described in [90], was verified at the MGH in terms of beam data for open and wedged beams and dose in a heterogeneous phantom under the clinical acceptance level of 5%. 3D dose was scored in a 5 mm x 5 mm x 5 mm grid which was exported in a DICOM format. Calculation took less than a minute per plan.

3.8.2 Calculation by MC

A Monte-Carlo (MC) system directly simulates physical interactions between particles which lead to energy deposition in a medium. Particles are transported in a medium random-wise: a random-number generator in a MC simulation code samples an interaction cross-section for a given medium to determine the type of interaction and the distance to the next interaction point.

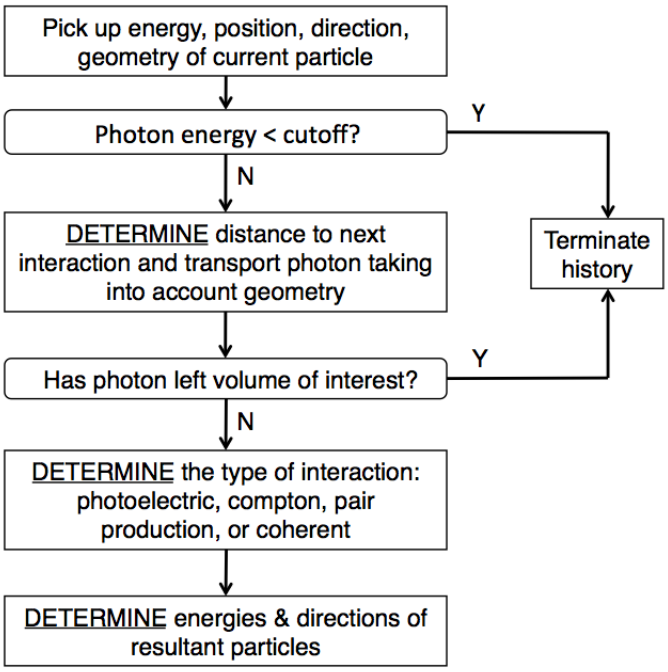

Figure 3.7: Flowchart of a MC simulation of photon transport. DETERMINE means that the parameter of the event is found by sampling from an relevant probability distribution. Reproduced from [91].

User-defined cutoff energies (ECUT for electrons, PCUT for photons) are defined below which the particle transport is terminated. Figure 3.7 summarizes the steps for MC simulation of photon transport.

The EGSnrc code system (2008 release) was used for the simulation of particle transport [92] and MMCTP (McGill Monte Carlo Treatment Planning) [93] to extract and visualize patient treatment plans on graphical user interface (GUI). EGSnrc system consists of BEAMnrc for simulation of radiation beams produced in linear accelerators and DOSXYZnrc for particle transport through the patient geometry.

Phase-space file generation by BEAMnrc: In order to run the BEAMnrc, an accelerator model, or beam model, needs to be specified. A beam model is an ordered set of component modules (CMs) each of which specifies the geometric shape of the actual accelerator component to be modeled. The

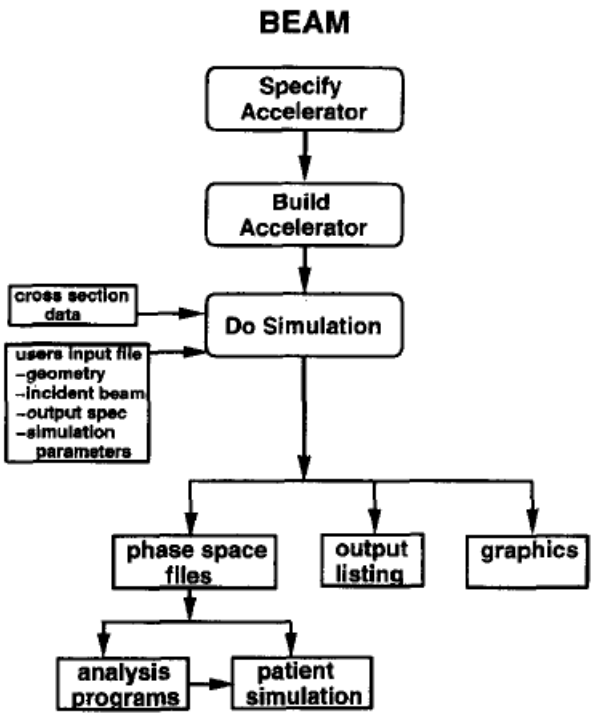

Figure 3.8: Flowchart of the processes to obtain a phase-space file in the BEAMnrc platform. Reproduced from [94].

beam model was commissioned by testing the accuracy of calculated dose profiles and central-axis percent depth dose (PDD) curves in a water phantom (figure 3.9, figure 3.10). A BEAMnrc input file contains the geometric specification of each CMs in the beam model which is retrieved from treatment plans and simulation control parameters related to statistics improvement or approximation. The simulation was run using the input file with global cutoff energies of ECUT = 0.700 MeV and PCUT = 0.010 MeV and a cross-section data set to generate a phase-space file on a scoring plane located at 70 cm from an electron source. A phase-space file contains information about particle position, direction, charge, etc. for every particle crossing a scoring plane. Typical simulation time for creating one phase-space file for 50 million particles was between 2 to 3 hours with 8 x 2.26 GHz processors.

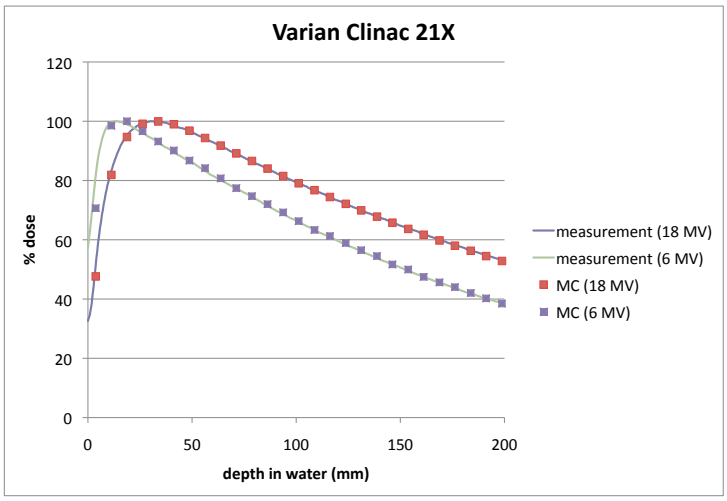

Figure 3.9: Comparison of percent depth dose along the central axis between ion-chamber measurement (straight lines) and Monte-Carlo (MC) simulation (squares) of a 10 X 10 cm photon beam from the Varian Clinac 21 X linear accelerator.

Patient dose calculation by DOSXYZnrc: Phase-space files generated for a treatment beam is used as a source of particles incident on patient body. The particles are transported in the patient body in the same manner as in the accelerator head. The patient geometry was represented in a 3D cubic grid (5 mm x 5 mm x 5 mm) that contained the information about the type of medium in each voxel. The segmentation of patient body into 4 materials (air, lung, tissue, bone) was performed using a CT-to-electron density calibration curve and a look-up table for material specification with known electron density ranges for different patient tissues. Different cross-section data were assigned to each medium, which inherently enabled heterogeneity correction. Local energy deposition in each voxel was scored in units of Gy/particle which was rescaled to Gy by multiplying a calibration factor achieved from standard open-beam simulation [4] and the number of MUs delivered per beam. Calculation was carried out with the sufficient number of particle histories to

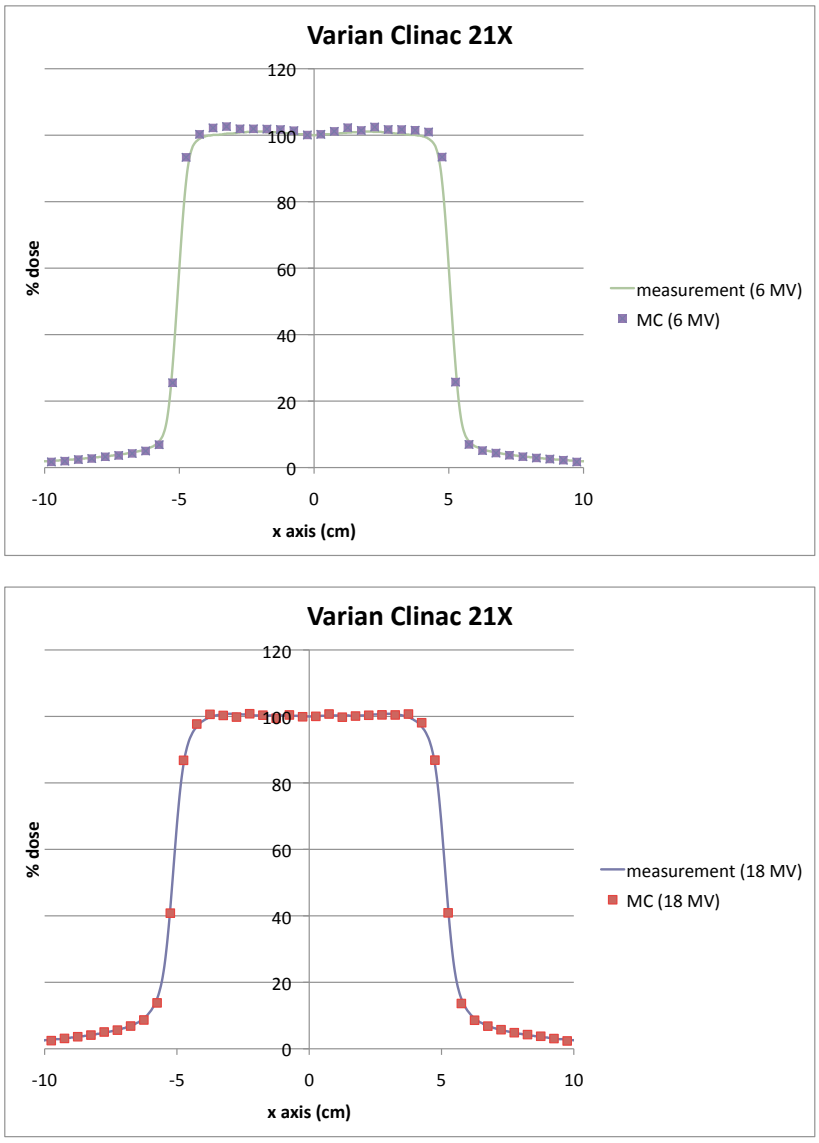

Figure 3.10: Comparison of dose profiles at the depth of dose maximum between ion-chamber measurement (straight lines) and Monte-Carlo (MC) simulation (squares) of a 10 X 10 cm photon beam from the Varian Clinac 21 X linear accelerator.

achieve clinically acceptable dose uncertainty (under 2% within the target). The required simulation time per beam was 2 to 3 hours on average.

3.9 Dose-injury correlation study

The dose distribution from AAA or MC, originally in 5 mm × 5 mm × 5 mm isotropic resolution, was resampled into the resolution of the corresponding planning CT image. The voxel locations for the injury segmentation were back-projected onto the planning CT. Using the resampled dose distribution, differential dose-volume histograms for the planning CT lung segmentation as well as the the corrected injury segmentation were created separately for a contralateral and ipsilateral lung as dose was binned from 0 to 60 Gy into 5 Gy intervals. The probability of complication for the ipsilateral or contralateral lung as a function of dose was defined according to [16]:

$$P(D_i) = \frac{N(injr, D_i)}{N(lung, D_i)} \tag{3.5}$$

where $N(injr, D_i)$ and $N(lung, D_i)$ are the number of voxels in the injury and lung segmentation, respectively, receiving the range of dose corresponding to a dose bin D_i. A set of $P(D_i)$ was obtained for each follow-up examination.

[4] Standard open-beam setup refers to a 10 cm × 10 cm square field to a water phantom at 100 cm SSD. The MC dose was sampled at 5 cm depth in phantom and scaled to the dose at d_{max}, depth at dose maximum, using a known PDD. A calibration factor was obtained as a ratio of a known beam output value to the scored dose at d_{max}.

CHAPTER 4
Results

4.1 overview

In this chapter, the time- and dose- dependence of RILD occurence to the 5 NSCLC patients were presented.

4.2 Image registration

Visual inspection on the matching of lung volumes between planning and follow-up CT image sets demonstrates that stretching of inferior lung due to inspiration was not fully corrected (figure 4.1). This results from the limitation of affine registration which permits global matching but not local flexibility. The effect of the local registration error on dose-injury correlation is assessed in the appendix A.1.

Registration accuracy for every follow-up CT image, evaluated in terms of lung contour DTA, was shown in the table 4.1. Note that each DTA value is an average of in-slice DTA only within the superior-inferior range of the scored RILD volume. Therefore, the DTA index reflects the registration error local to the RILD volume. The average DTA from all patients was 3.05/3.46/3.26 mm (ipsilateral/contralateral/whole lung), which were all under the voxel size of 3D dose matrices.

4.3 RILD segmentation

The injury segmentation, initially obtained by density thresholding on the density difference image, had to be further corrected by the coincidental

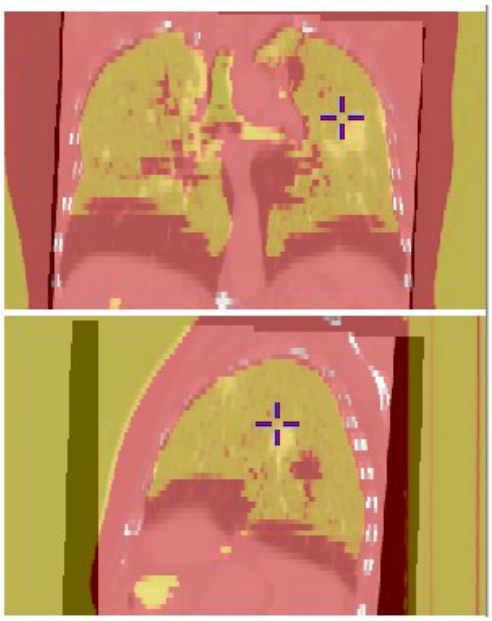

Figure 4.1: Example of affine registration showing anisotropic registration accuracy. Lung volumes from a target image (yellow) and a registered source image (dark red) are overlayed in a coronal (top) and a sagittal (bottom) view.

Patient no.	DTA (mm) (ipsi./cont.)					
	Post1	Post2	Post3	Post4	Post5	average
1	2.98/3.87	3.33/3.26	2.40/2.18	1.91/2.52	2.15/2.66	2.55/2.90
2	3.20/3.12	3.52/5.16				3.36/4.14
3	3.43/3.09	2.60/2.91	4.81/3.55			3.61/3.18
4		4.55/3.67	3.94/5.5			4.25/4.59
5	1.23/2.54	2.90/1.96	3.13/2.61	3.14/3.37		2.40/3.44

Table 4.1: Distance-to-agreement (DTA) between ipsilateral (ipsi.) and contralateral (cont.) lung contours drawn on a planning CT image and registered post-treatment (Post1∼Post5) CT images.

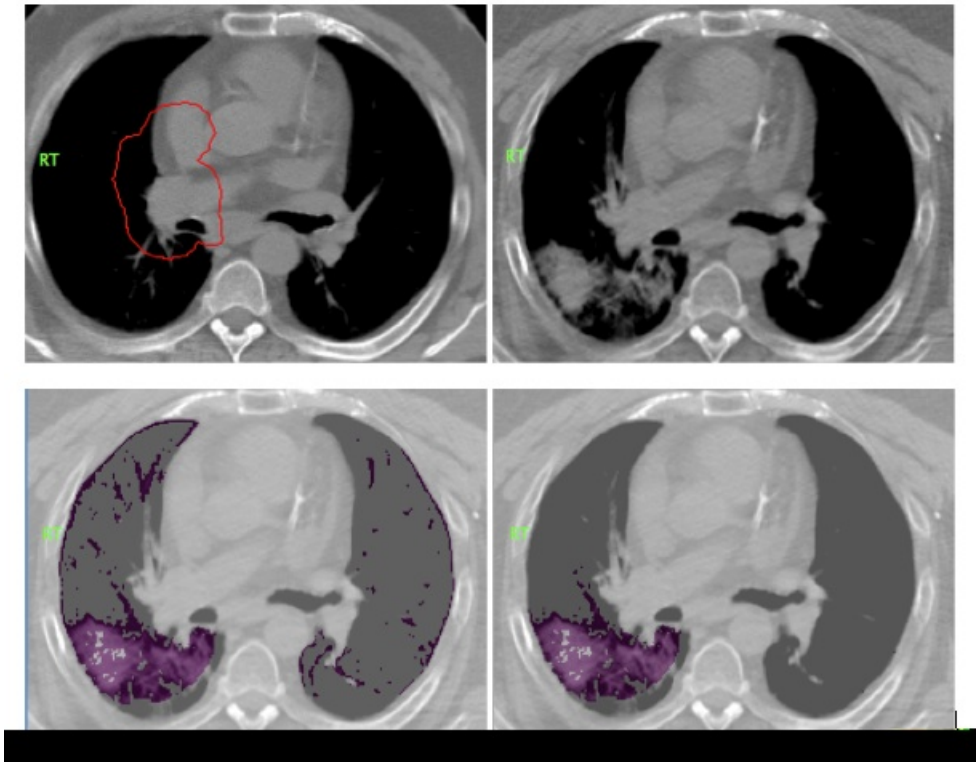

Figure 4.2: Injury segmentation (shown in purple) based on the physical density difference between the planning CT (top left: PTV contoured in red) from the post-RT CT (top right) included the small and isolated misaligned voxels which are clearly distinguishable from radiation pneumonitis in right-posterior lung (bottom left). Interactive correction on injury segmentation produced the final injury segmentation (bottom right).

segmentation of normal tissue features (lung periphery, blood vessels, bronchioles) because registration error often exceeded a size of a single voxel (figure 4.2).

4.4 Dose calculation

Average dose to the segmented lung, calculated using AAA or MC methods, is summarized in the table 4.2. Statistical uncertainty on the average dose from the DOSXYZnrc simulation was 4.23% for ipsilateral and 6.87% for contralateral lung. Significant difference in mean dose due to calculation engine, where the % difference exceeds the statistical uncertainty from MC,

Patient no.	$\overline{D}_{ipsi}$(Gy)			$\overline{D}_{cont}$(Gy)		
	MC(unc.)	AAA	MC-AAA(%)	MC(unc.)	AAA	MC-AAA(%)
1	16.85 (8.25)	16.92	-0.39	13.51 (9.16)	13.45	0.44
2	24.11 (5.05)	24.61	-2.08	10.45 (9.05)	10.78	-3.16
3	20.71 (2.73)	20.36	1.69	10.93 (4.01)	10.43	4.51
4	32.27 (2.02)	33.52	-3.87	5.77 (6.22)	6.10	-5.72
5	21.72 (3.12)	22.55	-3.82	7.91 (5.66)	8.40	-6.20

Table 4.2: Average dose to the segmented ipsilateral (ipsi) and contralateral (cont) lung using MC or AAA calculation engines. Dose uncertainties from MC (unc.) and MC-AAA difference are shown in percentage of MC dose value.

was occasionally noted (contralateral lung for patient 3 and 5, ipsilateral lung for patient 4 and 5).

4.5 Post-RT dependence of RILD volume

The segmented RILD volume demonstrated patient variability and high post-RT time dependence (figure 4.3). Much less damage was inflicted to contralateral side than the ipsilateral. With regard to the time-dependence, for most of the cases the suppression of the damage between 100 and 150 days after the RT was observed, which was followed by stabilization beyond 150 $\sim$ 200 days. The exact onset of RILD was not clear due to the lack of follow-ups up to 3 months after RT. Nevertheless, latency was observed for patient 4 while the response was immediate for patient 5.

4.6 RILD-local dose correlation

The probability of developing RILD is plotted against local dose for each follow-up studies, shown in figures 4.4, 4.5, 4.6, 4.7, and 4.8. These dose-response curves graphs again confirm the time- and patient- dependence of the normal tissue response which were shown in the section 4.5. The magnitude of the response was generally reduced in time with an exception of patient 5 where a significant increase in probability at dose $>$ 45 Gy was observed at 543 days post-RT (4.8(c)) in comparison to 389 days (4.8(b)). The presence

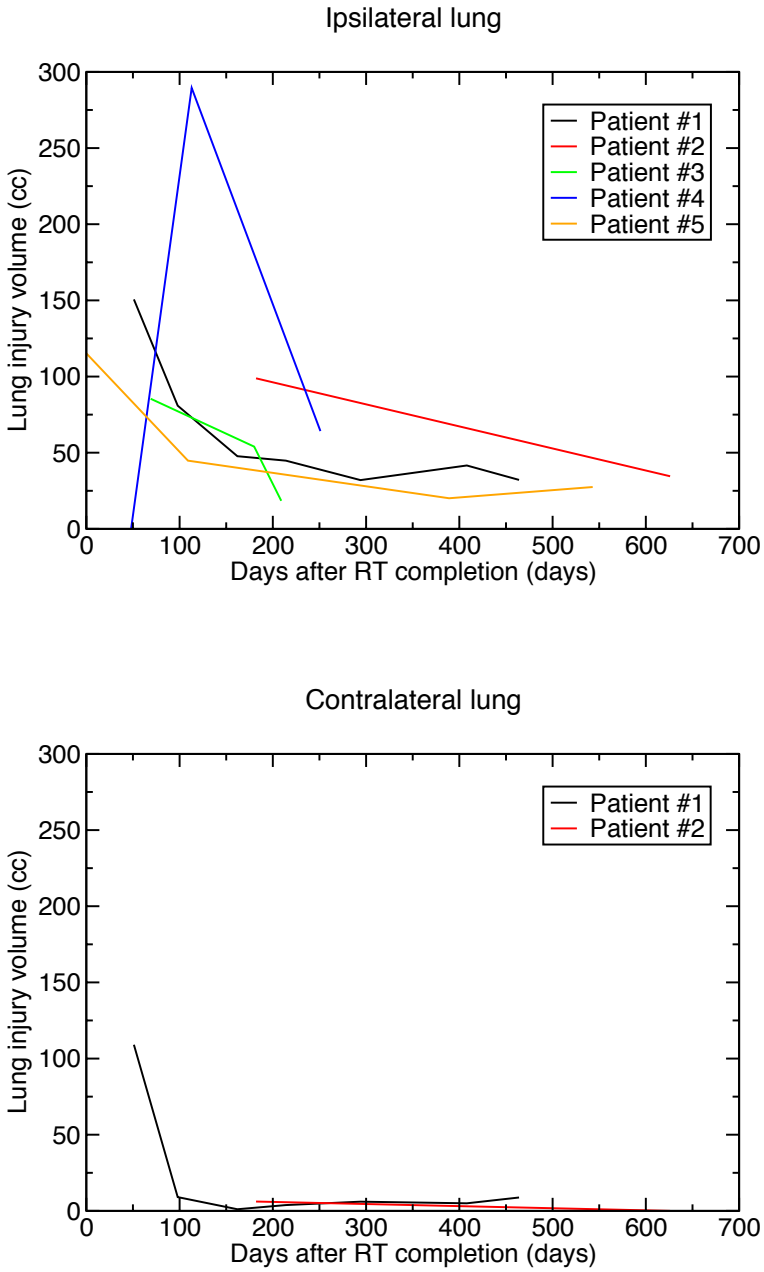

Figure 4.3: Changes of the volume of the scored RILD in ipsilateral (top) and contralateral (bottom) lung as a function of post-RT time for all patients.

Follow-up class	r_s/p-value	
	AAA dose	MC dose
Early	$0.817/< 5*10^{-}4$	$0.832/< 5*10^{-}4$
Intermediate	$0.778/< 5*10^{-}4$	$0.788/< 5*10^{-}4$
Late	$0.701/< 5*10^{-}4$	$0.671/< 5*10^{-}4$

Table 4.3: Spearman's coefficients (r_s) and associated p-values for local injury-dose correlation from all patients, classified into the three observation periods (early, intermediate, and late).

of a threshold dose is another common feature for the follow-up studies later than 120 days. Nevertheless, 2 of early observation (4.4(a) and 4.7(a)) demonstrate linear-no-threshold (LNT) resembling dose responses. There was slight modification in the response curves by using different dose engines, which occasionally produced significant shifts (figure 4.6(a), figure 4.6(c), figure 4.7(a), and figure 4.7(b)).

4.7 Strength of correlation

The strength of local injury-dose correlation was quantified using a spearman's coefficient[1] , r_s, and its dependence on follow-up timing and dose calculation was investigated. Firstly, each dose-response curve was classified according to its post-RT days into early (< 100 days), intermediate (100 days ~ 200 days), and late (> 200 days) follow-ups. For each class, the data from the 5 patients were combined in which r_s for AAA or MC dose and their associated p-values were calculated. Table 4.3 suggests, regardless of dose calculation methods, that the strength of the local correlation diminished as the observation was taken at later time.

[1] Spearman's rank coefficient, r_s, is a measure of the linear correlation between two ranked variables. It can be used to describe how monotonic a given relationship between two variables is. r_s ranges between -1 and 1, where an absolute value represents a strength of monotonicity and a sign indicates the direction of association between the variables.

Patient no.	r_s/p-value	
	AAA dose	MC dose
1	$0.675/< 5*10^{-}4$	$0.655/< 5*10^{-}4$
2	$0.898/< 5*10^{-}4$	$0.898/< 5*10^{-}4$
3	$0.677/< 5*10^{-}4$	$0.809/< 5*10^{-}4$
4	0.544/0.004	$0.691/< 5*10^{-}4$
5	$0.795/< 5*10^{-}4$	$0.803/< 5*10^{-}4$

Table 4.4: Spearman's coefficients (r_s) and associated p-values for local injury-dose correlation for each of 5 patients.

Since patient dose calculation is specific to a treatment plan and patient geometry, the dose-response curves from the same patient were combined so as to examine the dependence of r_s on dose calculation methods (table 4.4). For the majority of the patients, local injury correlated more strongly with MC than AAA dose distribution (patient 3,4, and 5). However, the difference in those correlation coefficients were not statistically significant at 95% confidence level revealed by Student's t-test (t-value: 0.712).

4.8 Uncertainty analysis

Aforementioned methods of dose-RILD correlation study were critically evaluated by estimating uncertainties on dose-response relationship, $P(D_i)$, which arises due to the fitting of measurements to theoretical models, poor statistics from random processes, or the lack of ground truth reference to serve as a benchmark. Understanding the sources of uncertainties is important, not only to use the toxicity data with precaution, but also to identify what techniques have to be improved to produce more accurate and reproducible results. The following three main procedures were determined as the factors that significantly influence the uncertainty on the $P(D_i)$:

1. Image registration.
2. CT calibration.
3. Dose calculation.

Source procedure	Mean	Standard deviation	Median	Range
registration (affine)	1.77	1.89	1.25	0∼8.44
CT calibration	1.93	1.91	1.52	0∼11.60
Dose calculation (MC)	0.80	1.37	0.38	0∼9.07
Total	3.48	2.82	2.71	0∼18.60

Table 4.5: Statistics of uncertainties on $P(D_i)$ from the three main sources. Numbers shown in percentage complication probability.

Uncertainties on dose-response curves, shown in error bars on the graphs 4.4, 4.5, 4.6, 4.7, and 4.8, were estimated using the procedures which are stated in the appendix. Table 4.5 reveals the average uncertainty of 3.5% and suggests that CT calibration creates the largest uncertainty which is closely followed by image registration.

4.9 Summary

Post-RT CT images were registered to the corresponding planning CT image with the average accuracy of 3.26 mm for an area bounded by the extended of the scored RILD. Local mismatch between the source and target lung volumes, predominantly in lung based, was often observed. The extent of RILD was initially determined based on physical density change, which had to be corrected manually due to mismatch of normal high-density anatomical structures. Patient dose calculation occasionally demonstrated significant difference in MLDs between MC and AAA methods. The total RILD volume was patient- and time-specific. Marked decrease in the volume before 200 days after RT followed by stabilization was common for all the patients. The relationship between local dose and the probabilities for injury was again specific to post-RT time and patients. From those time-varying dose-response curves, transition from linear-no-threshold to nonlinear-with-threshold behaviour as

well as decrease in correlation strength were noted as the patients were examined at later time. Dose from the MC method showed stronger correlation than the AAA counterpart. The uncertainty in $P(D_i)$, varying with dose bins and follow-up images, was 3.5% on average with CT calibration and image registration as the two main contributors.

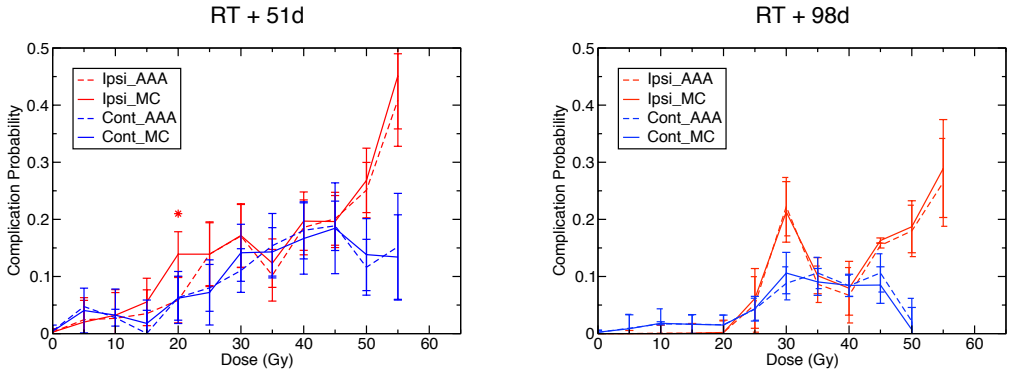

(a)

(b)

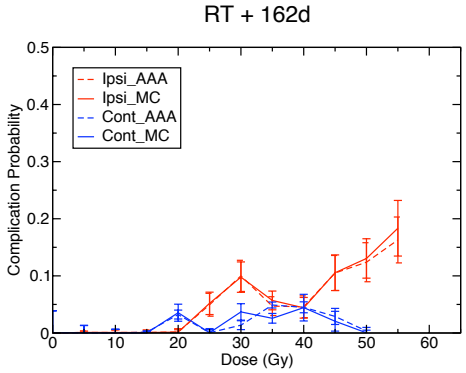

(c)

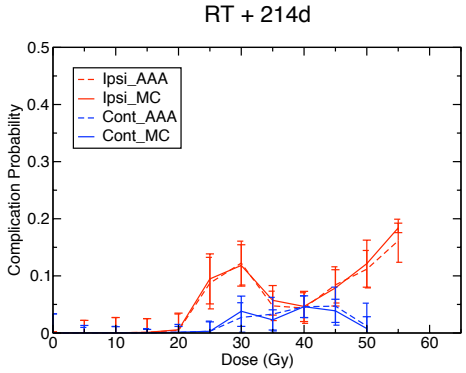

(d)

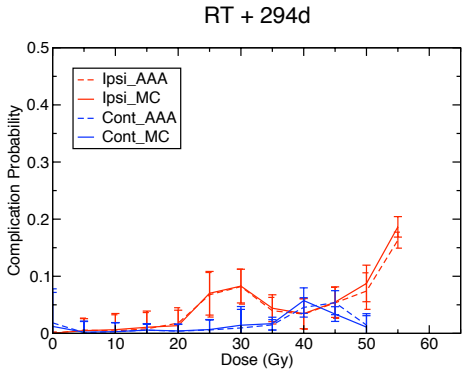

(e)

Figure 4.4: Dose-response curves for ipsilateral (red) and contralateral (blue) lung of patient 1. Figure 4.4 $\sim$ Figure 4.8: Correlation with MC and AAA dose shown in straight and dotted lines, respectively. Error bars are combined uncertainties (see the appendix). Asterisks(*) denote the dose bins where the probability obtained from MC dose is significantly different from AAA dose.

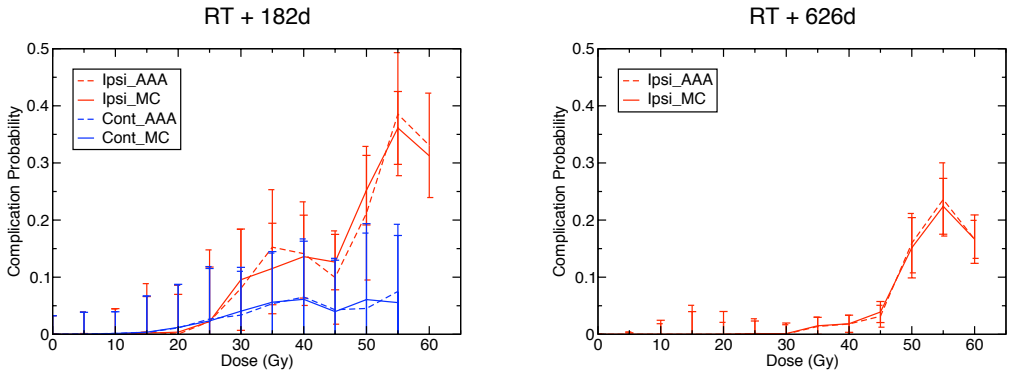

(a) (b)

Figure 4.5: Dose-response curves for ipsilateral (red) and contralateral (blue) lung of patient 2.

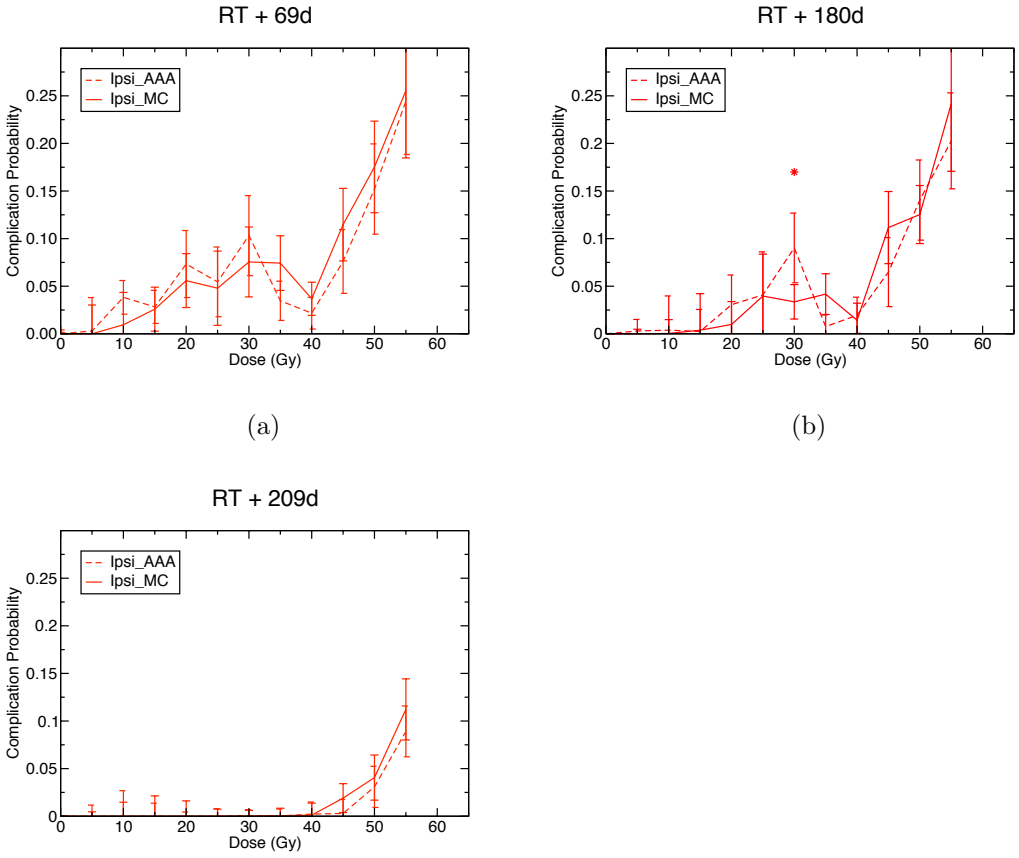

(a) (b)

(c)

Figure 4.6: Dose-response curves for ipsilateral lung of patient 3. No injury was found in contralateral lung.

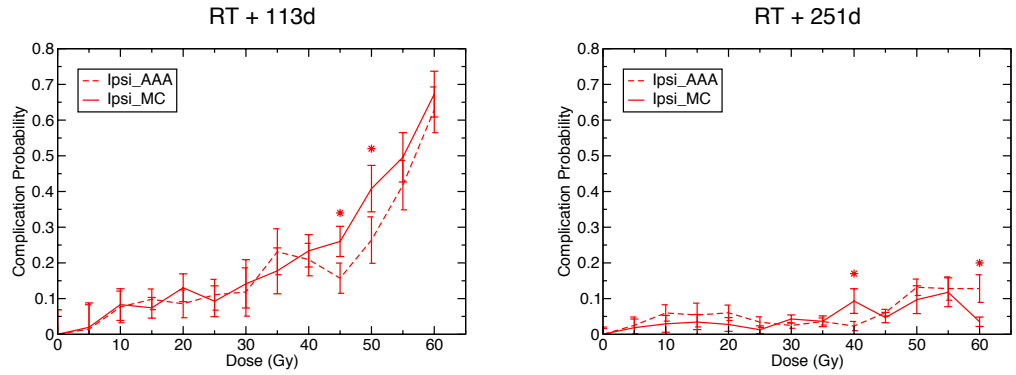

(a) (b)

Figure 4.7: Dose-response curves for ipsilateral lung of patient 4. No injury was found in contralateral lung.

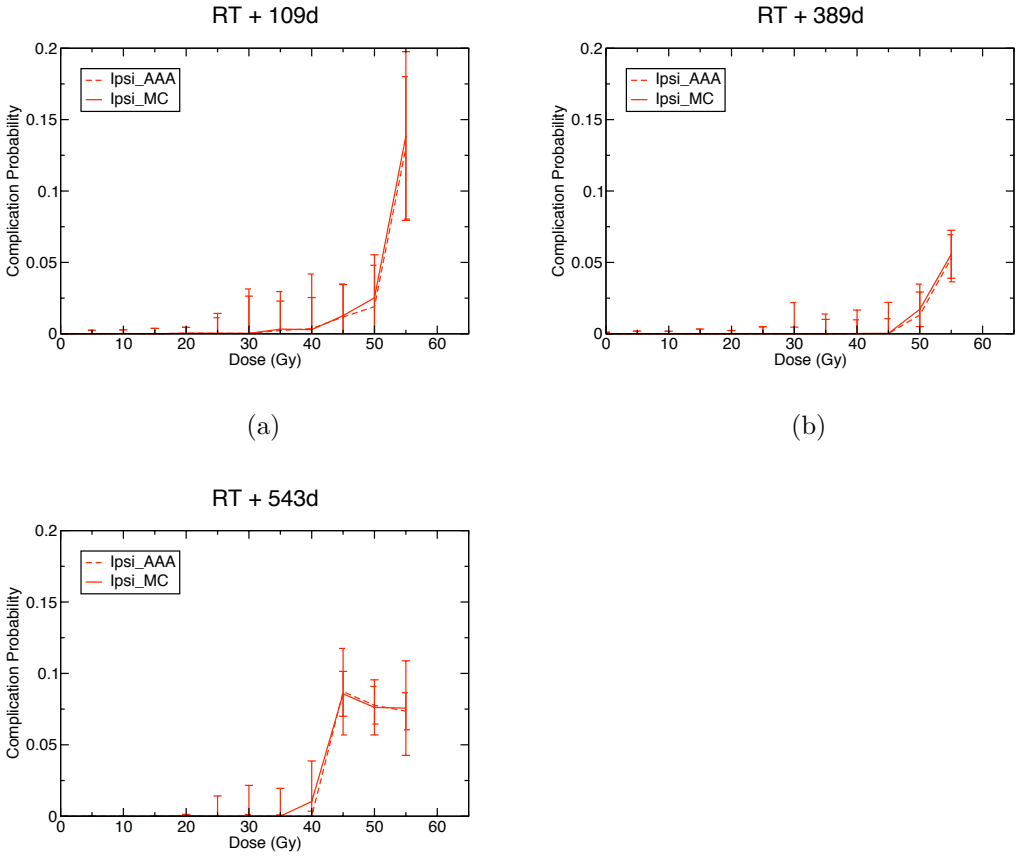

(a) (b)

(c)

Figure 4.8: Dose-response curves for ipsilateral lung of patient 5. No injury was found in contralateral lung.

CHAPTER 5
Discussion

This study identified a patient-specific relationship between lung tissue damage and post-treatment time or local dose deposition. It is apparent that inhomogeneity of the patient group such as different chemotherapy regimens caused inter-patient variation although prescription dose and fraction, identified as the most significant determinants of lung fibrosis [95], were controlled. Nevertheless, 4 out of 5 patients commonly demonstrated transition from linear-no-threshold to nonlinear-with-threshold type dose response. This implies the presence of two distinct disease phases - pneumonitis and fibrosis - and the timing of the transition from pneumonitis to fibrosis, corresponding to the onset of the stabilization of injury volume after 150 days post-treatment (figure 4.3), correlates well with literature [24]. Also, threshold dose values ranging from 30 to 40 Gy was also consistent with previous radiation-induced fibrosis studies ([95], [15], [16]).

Up to date, there has been no consensus as to whether lung has to be considered as an individual organ or a paired organ for evaluating equivalent average dose [48]. Oetzel et al. [46] found that RP risk predicted based on MLD did not significantly depend on whether the analysis was performed as a paired or an individual organ. On the other hand, Yorke et al. [96] suggested the correlation between MLD and RP risk was stronger when lung was separated into ipsilateral and contralateral lung. This study revealed the significant difference in response between ipsilateral and contralateral lungs for all patients. Primary reason is the location of the target: Most of the

target volume was located laterally except for one case (patient 1) for which contralateral lung showed significant response (figure 4.4). The absence of response weakly suggests the presence of threshold dose-volume parameters under which no structural damage is inflicted, although more patients with various tumor positions should be included to verify this. Nevertheless, we found that the paired lung model is more realistic not to underestimate the probability of local damage by analyzing the lung as a whole.

By comparing Spearman's coefficients, it was noted that the probability for injury correlates stronger with MC dose than AAA dose, although a larger group of patients is needed to show the statistical significance of the difference. This observation conforms to that from Stroian et al. [16] who compared dose-fibrosis relationship from MC against pencil-beam based CadPlan dose without heterogeneity correction. Similarly, Jaeger et al. [97] showed that the correlation between observed and calculated pneumonitis risk based on DVH parameters was stronger when the DVH was calculated with convolution-superposition (CS) based algorithm than equivalent-path-length (EPL) algorithm. These studies represent the evidence that accurate dose calculation is important in accurately assessing the risk of normal tissue complication. Although the DVH-based prediction was out of the scope of this study due to the limited number of patients, we expect that MC-derived DVH parameters would also lead to different RILD risk to the conventional equivalents because MC simulation occasionally yielded significantly different MLDs than AAA calculation (table 4.2).

Previous image-based lung injury scoring and dose-correlation studies ([95], [15], [14], [16]) did not explicitly examine how the random errors that can arise from any steps of their analyses can affect the correlation. For the first time, this study systematically estimated the uncertainty on dose-response

curves for every patients by modeling the extreme-case deviations at which local correlation analysis is repeated. Although the rigorousness of assuming extreme deviations can be questioned, it was possible via this systematic approach to rank three main processes - image registration, CT calibration, and dose calculation - according their significance in creating uncertainties and identify which processes need improvements in the degree of accuracy.

The largest contributor was CT calibration (table 4.5). According to the equation A.4, the uncertainty from the CT calibration can be reduced by acquiring more precise calibration parameters. The uncertainties in the parameters are attributed to inter-patient variation in the calibration function which is due to different patient size that would alter beam quality by beam hardening and actual variation in the physical densities of tissues to be sampled. Therefore, rather than sampling from the actual patient images which are patient specific, obtaining CT numbers from scanning a standardized phantom is expected to enhance the precision of CT calibration and subsequently dose-correlation studies.

The purpose of image registration is twofold: 1) to be able to locate injured voxels by subtracting two CT images in the reference frame, and 2) align dose distribution which is calculated in the reference frame with respect to anatomical change. The first purpose was partially achieved yet with demand for manually removing the voxels that are not relevant to injuries. Therefore, in the future, inter-observer variation in the manual correction of RILD segmentation needs to be included in the total uncertainty. How well the registration fulfilled the latter purpose was tested by applying a perturbation on the alignment optimized by the registration algorithm. Figure A.1 demonstrates that the change in correlation is dramatic when the shift is applied in the superior-inferior direction. Finding the correct superior-inferior

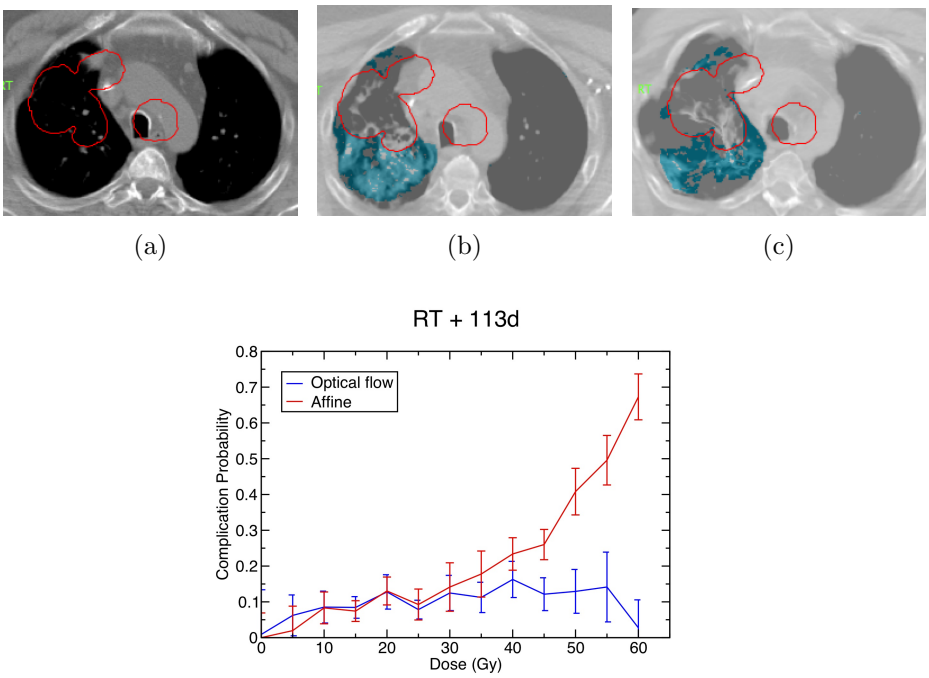

Figure 5.1: Comparison of the performance of affine against deformable (optical flow) registration using algorithm in the presence of pneumonitis volume in the right posterior lung. (a) a target image with PTV contoured in red. (b) a registered source image using affine algorithm. injury identified in blue. (c) the same source image registered with optical flow algorithm. (d) dose-response of lung registered with affine algorithm (red) and optical flow algorithm (blue).

alignment is crucial because of steep dose gradient created by coplanar beam setups. Deformable registration is expected to be superior to affine registration in reproducing lung deformation which is predominantly in superior-inferior direction. However, there is a need for a new algorithm which is robust against abrupt anatomical changes as many of current deformable algorithms assume small changes in brightness or deformation [62] [64]. Figure 5.1 demonstrates that an ordinary optical flow algorithm underperforms affine registration under the presence of a pneumonitis volume in terms of contour matching of the right lung and the strength of the resulting dose-correlation.

The primary limitation of this study comes from the fact only anatomical information from CT images was considered for identifying RILD. Injury segmentation based on physical density lacks specificity to radiation-induced change, which is a major challenge near the primary site in differentiating RILD from recurrent tumor [9]. For this reason, the whole PTV volume was rejected from the region of interest where the RILD was scored. This caused an underestimation of the total injury volume and also limited the investigation of the dose response to less than 60 Gy. PET imaging is a potential solution to the lack of specificity by adding functional information to the segmentation criteria. In this study, however, most of the PET scans were acquired 3 months after the completion of RT when the differentiation between RILD and malignancy is known to be difficult due to high activity in pneumonitis [17] [18] [19] [20].

A second question lies in the clinical relevance of a radiological endpoint to quantify lung toxicity because it does not necessarily correlate with other endpoints: Radiologic pneumonitis occurs more often than symptomatic pneumonitis [24] [25], which was the case for our patient group (table 3.1). Also, dose-dependency of local physical density increase does not coincide with the functional dependence of dose to local perfusion or ventilation change [98] [14]. Further studies are needed to correlate the sum of regional damage to the change in the whole organ function.

Another criticism we expect is the simplicity of the physical model of lung we used. In this study, lung was assumed to be a completely parallel organ: that is, regional damage of one region of lung, partitioned into CT voxels, is completely independent of the state of other region, and every voxel is considered equivalent in its dose-response behavior. Therefore, effective radio-responsiveness of the whole organ (ipsilateral or contralateral lung) was

characterized by the dose-dependent frequencies of injury incidences on those equally-weighted voxels. However, animal and human studies suggests the existence of spatial heterogeneity in lung radiosensitivity [38] [39] [40]. In the parallel or critical volume model, density and size of FSU (acini for lung) are important parameters in determining the regional sensitivity of an organ [99]. A possible explanation from this model is that the lung base contains more acini per volume than lung apex [100]. Methods from this proposed study can be applied to investigate the regional sensitivity on a larger patient dataset with variable superior-inferior tumor positions.

CHAPTER 6
Conclusions and Outlook

The biggest advantage of using radiographic images to score endpoints for normal tissue toxicity is its objectiveness and reproducibility as compared to symptom-based scoring which is relatively subjective [101] and often affected by confounding medical conditions [23] [102]. Moreover, due to the prevalence of radiologic change relative to clinical symptoms, larger number of patients are available for study. Toxicity data acquired by consistent and accurate means can be used to prospectively evaluate radiotherapy treatment plans with respect to the forecast risk for complication.

This thesis outlined an objective and semi-automatic method of scoring radiographically-defined RILD from CT image analysis and retrospectively applied the method to a group of NSCLC patients to provide the relationship between RILD and local dose. Normal lung tissue response in terms of RILD volume and local dose-response showed significant dependency on post-RT time and patients. The uncertainty analysis revealed that the ability of this tool to accurately score RILD and correlate with local dose depends on the quality of CT calibration and image registration with an appropriate algorithm. By comparing the strength of local dose-RILD correlation with a conventional dose calculation model, the importance of Monte-Carlo dose calculation on normal tissue toxicity studies was again emphasized.

The presented responses of the 5 patients to radiotherapy may not have clinical significance due to small sample size. However, the methods presented in this thesis can be applied to the larger number of patients to reveal the

correlation with other clinically relevant variables such as tumor positions or chemotherapy regimen. These can be extended to analyzing multi-modality images to complement the limitation of the anatomical radiographic endpoints. By these efforts, more realistic relationship can be established between patient and treatment information and the outcome of the treatment.

APPENDIX A
Uncertainty Analysis

A.1 Overview

This section includes detailed methodology to estimate the uncertainty on $P(D_i)$ from the three main contributors:

1. Image registration.
2. CT calibration.
3. Dose calculation.

A.2 Image registration

Due to the difficulty to identify ground-truth voxel correspondence, there is the uncertainty on the goodness of alignment between injury distribution and dose distribution. It was assumed that the current alignment was shifted to the "true" alignment in any direction by the distance of an isotropic registration error. Thus, dose distribution was shifted with respect to injury distribution in six directions (left, right, anterior, posterior, superior, and inferior) by the registration error evaluated from contour DTA (table 4.1), and dose-injury correlation was recalculated for each direction of shift (Figure A.1). Fluctuation of the correlation due to the dose shift was measured by the standard deviation of seven $P(D_i)$ values for a given dose bin D_i, which is uncertainty contribution from image registration ($\sigma_P^R(D_i)$).

It was previously stated that image mismatching leads to errors in injury segmentation 4.2. Manual correction on clearing mis-segmentation was applied. Estimation of uncertainty from this procedure was difficult to assess because the number of observers was not enough to validate observer dependency. Although not revealed in this thesis, the true uncertainty from image

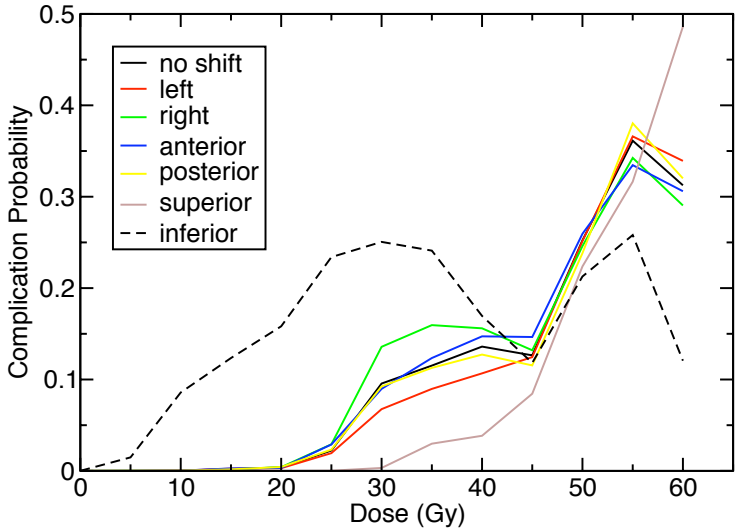

Figure A.1: Demonstration of the change of one dose-response curve due to the shift of dose distribution by registration accuracy (3.2 mm). Note the dramatic change in correlation as a result of superior-inferior shifts.

registration has to include the variability of the manual correction between multiple observers.

A.3 CT calibration

CT calibration establishes the empirical relationship between physical density and pixel value represented by two pairs of calibration parameters (a_L, b_L, a_H, and b_H):

$$\rho = a_L HU + b_L \quad (HU < 50) \tag{A.1}$$

$$= a_H HU + b_H \quad (HU > 50) \tag{A.2}$$

Uncertainties on CT calibration parameters due to data fitting and patient averaging $(\sigma_{a_L}, \sigma_{b_L}, \sigma_{a_H}, \sigma_{b_H})$, shown in figure 3.6, can be passed onto the uncertainty on converted density via error propagation principles:

$$\sigma_\rho^2 = (\frac{\partial \rho}{\partial a})^2 \sigma_a^2 + (\frac{\partial \rho}{\partial (HU)})^2 \sigma_{HU}^2 + (\frac{\partial \rho}{\partial b})^2 \sigma_b^2 \tag{A.3}$$

After uncertainty on pixel values is ignored and partial derivatives are evaluated:

$$\sigma_\rho^2 = HU^2 \sigma_a^2 + \sigma_b^2 \tag{A.4}$$

Thus, the density uncertainty is HU-dependent, which amounts to $\sim 0.013 g/cm^3$ for the lowest ($\rho_l = 0.123\ g/cm^3$) and $\sim 0.008\ g/cm^3$ for the highest ($\rho_u = 0.799\ g/cm^3$) density thresholds for the RILD segmentation. This means that, under 95% confidence, the true RILD segmentation range to be applied to the density image lies between $[\rho_l - 0.026\ g/cm^3,\ \rho_h + 0.016\ g/cm^3] \sim [\rho_l + 0.026\ g/cm^3,\ \rho_h - 0.016\ g/cm^3]$. Now, the injury segmentation was repeated twice with those modified segmentation thresholds (figure A.2), and the standard deviation of the three $P(D_i)$ values was estimated as uncertainty contribution from the calibration process ($\sigma_P^C(D_i)$).

A.4 Dose calculation (MC dose only)

Dose uncertainty($\sigma_D(D_i)$) from MC simulation, assumed to be uniform within the each side of lung (table 4.2), was propagated into the equivalent uncertainty on the complication probability ($\sigma_P^D(D_i)$) via the following equation:

$$\sigma_P^D(D_i) = |\frac{\partial P(D_i)}{\partial D_i}| \sigma_D(D_i) \tag{A.5}$$

A.5 Total uncertainty

It was assumed that the three sources of uncertainties (image registration, CT calibration, dose calculation) are independent processes. Under this assumption, total uncertainty on $P(D_i)$, $\sigma_P(D_i)$, was calculated by combining

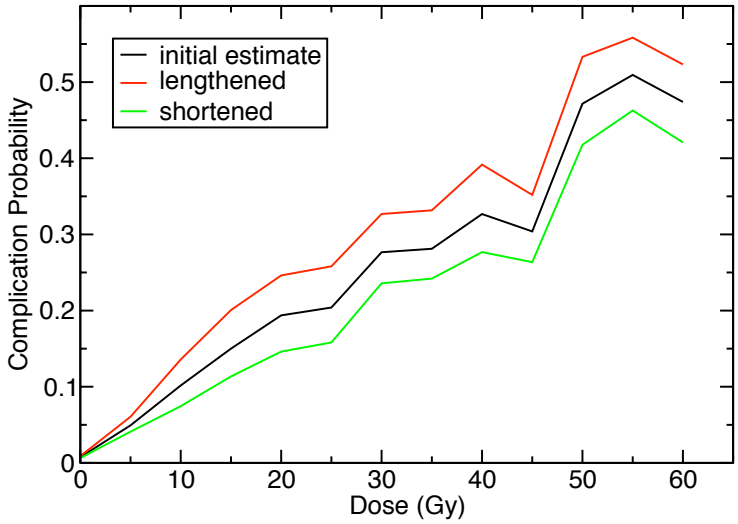

Figure A.2: Demonstration of the change of one dose-response curve due to the uncertainty in calibrated physical density. "Lengthened" and "shortened" denote the modified segmentation ranges, $[\rho_l - 0.026\ g/cm^3, \rho_h + 0.016\ g/cm^3]$ and $[\rho_l + 0.026\ g/cm^3, \rho_h - 0.016\ g/cm^3]$, respectively.

certainties from the three sources with covariance terms between the sources were ignored.

$$\sigma_P(D_i) = \sqrt{\{\sigma_P^R(D_i)\}^2 + \{\sigma_P^C(D_i)\}^2 + \{\sigma_P^D(D_i)\}^2} \tag{A.6}$$

It should be noted that the $\sigma_P(D_i)$ above does not include potential uncertainty from RILD scoring due to image registration error.

REFERENCES

[1] Canadian Cancer Society. *Canadian Cancer Statistics 2009*. Canadian Cancer Society, 2009.

[2] Scott Tyldesley, Chris Boyd, Karleen Schulze, Hugh Walker, and William J. Mackillop. Estimating the need for radiotherapy for lung cancer: an evidence-based, epidemiologic approach. *International Journal of Radiation Oncology*Biology*Physics*, 49(4):973 – 985, 2001. ISSN 0360-3016.

[3] Jatinder R. Palta, T. Rockwell Mackie, and Zhe Chen. Intensity-Modulated Radiation Therapy—The State of the Art. *Medical Physics*, 30(12):3265–3265, 2003.

[4] E. J. Hall and A. J. Giaccia. *Radiobiology for the Radiologist*. Lippincott Williams and Wilkins, 2006.

[5] Graeme W. Morgan, B. Pharm, and Samuel N. Breit. Radiation and the lung: A reevaluation of the mechanisms mediating pulmonary injury. *International Journal of Radiation Oncology*Biology*Physics*, 31(2):361 – 369, 1995.

[6] Philip Rubin, Carl J. Johnston, Jacqueline P. Williams, Sandra McDonald, and Jacob N. Finkelstein. A perpetual cascade of cytokines postirradiation leads to pulmonary fibrosis. *International Journal of Radiation Oncology*Biology*Physics*, 33(1):99 – 109, 1995. ISSN 0360-3016.

[7] H.I.Libshitz and M.E.Southard. Complications of radiation therapy: the thorax. *Semin Roentgenol.*, 9(1):41–49, 1974.

[8] James D. Cox, JoAnn Stetz, and Thomas F. Pajak. Toxicity criteria of the radiation therapy oncology group (rtog) and the european organization for research and treatment of cancer (eortc). *International Journal of Radiation Oncology*Biology*Physics*, 31(5):1341 – 1346, 1995. ISSN 0360-3016. Late Effects of Normal Tissues (LENT) Consensus Conference.

[9] Titus R. Koenig, Reginald F. Munden, Jeremy J. Erasmus, Bradley S. Sabloff, Gregory W. Gladish, Ritsuko Komaki, and Craig W. Stevens. Radiation Injury of the Lung After Three-Dimensional Conformal Radiation Therapy. *Am. J. Roentgenol.*, 178(6):1383–1388, 2002.

[10] Herman I. Libshitz. Radiation changes in the lung. *Seminars in Roentgenology*, 28(4):303 – 320, 1993.

[11] Shirley Lehnert and Ellen El-Khatib. The use of ct densitometry in the assessment of radiation-induced damage to the rat lung: A comparison with other endpoints. *International Journal of Radiation Oncology*Biology*Physics*, 16(1):117 – 124, 1989. ISSN 0360-3016.

[12] Ellen el Khatib and Shirley Lehnert. Lung density change observed in vivo in rat lungs after irradiation: variations among and within individual lungs. *International Journal of Radiation Oncology*Biology*Physics*, 16:745–754, 1989.

[13] Michael I. Koukourakis, Pelagia G. Tsoutsou, and Ioannis Abatzoglou. Computed tomography assessment of lung density in patients with lung cancer treated with accelerated hypofractionated radio-chemotherapy supported with amifostine. *Americal Journal of Clinical Oncology*, 32: 258–261, 2009.

[14] Jinli Ma, Junan Zhang, Sumin Zhou, Jessica L. Hubbs, Rodney J. Foltz, Donna R. Hollis, Kim L. Light, Terence Z. Wong, Christopher R. Kelsey,

and Lawrence B. Marks. Regional lung density changes after radiation therapy for tumors in and around thorax. *International Journal of Radiation Oncology*Biology*Physics*, 76(1):116 – 122, 2010. ISSN 0360-3016.

[15] Isaac I. Rosen, Teresa A. Fischer, John A. Antolak, George Starkschall, Elizabeth L. Travis, Susan L. Tucker, Kenneth R. Hogstrom, James D. Cox, and Ritsuko Komaki. Correlation between Lung Fibrosis and Radiation Therapy Dose after Concurrent Radiation Therapy and Chemotherapy for Limited Small Cell Lung Cancer1. *Radiology*, 221 (3):614–622, 2001.

[16] Gabriela Stroian, Chandra Martens, Luis Souhami, D. Louis Collins, and Jan Seuntjens. Local correlation between monte-carlo dose and radiation-induced fibrosis in lung cancer patients. *International Journal of Radiation Oncology*Biology*Physics*, 70(3):921 – 930, 2008. ISSN 0360-3016.

[17] T Bury, JL Corhay, B Duysinx, F Daenen, B Ghaye, N Barthelemy, P Rigo, and P Bartsch. Value of FDG-PET in detecting residual or recurrent nonsmall cell lung cancer. *Eur Respir J*, 14(6):1376–1380, 1999.

[18] Abass Alavi, Naresh Gupta, Jean-Louis Alberini, Marc Hickeson, Lars-Eric Adam, Peeyush Bhargava, and Hongming Zhuang. Positron emission tomography imaging in nonmalignant thoracic disorders. *Seminars in Nuclear Medicine*, 32(4):293–321, 2002.

[19] Tomio Inoue, E. Edmund Kim, Ritsuko Komaki, Franklin C.L. Wong, Pedro Bassa, Wai-Hoi Wong, David J. Yang, Keigo Endo, and Donald A. Podoloff. Detecting Recurrent or Residual Lung Cancer with FDG-PET. *J Nucl Med*, 36(5):788–793, 1995.

[20] Siema Bahkeet, Mohamad Saleem, John Powe, Abdullah Amro, Sven Larsson, and Zeyad Mahassin. F-18 fluorodeoxyglucose chest uptake in lung inflammation infection. *Clinical Nuclear Medicine*, 25(4):273–278, 2000.

[21] Sandra McDonald, Philip Rubin, Theodore L. Phillips, and Lawrence B. Marks. Injury to the lung from cancer therapy: Clinical syndromes, measurable endpoints, and potential scoring systems. *International Journal of Radiation Oncology*Biology*Physics*, 31(5):1187 – 1203, 1995. ISSN 0360-3016. Late Effects of Normal Tissues (LENT) Consensus Conference.

[22] L. J. Boersma, E. M. F. Damen, R. W. de Boer, S. H. Muller, R. A. Valds Olmos, N. van Zandwijk, and J. V. Lebesque. Estimation of overall pulmonary function after irradiation using dose-effect relations for local functional injury. *Radiotherapy and Oncology*, 36(1):15 – 23, 1995. ISSN 0167-8140.

[23] Zafer Kocak, Elizabeth S. Evans, Su-Min Zhou, Keith L. Miller, Rodney J. Folz, Timothy D. Shafman, and Lawrence B. Marks. Challenges in defining radiation pneumonitis in patients with lung cancer. *International Journal of Radiation Oncology*Biology*Physics*, 62(3):635 – 638, 2005. ISSN 0360-3016.

[24] Yo Won Choi, Reginald F. Munden, Jeremy J. Erasmus, Kyung Joo Park, Woo Kyung Chung, Seok Chol Jeon, and Choong Ki Park. Effects of radiation therapy on the lung: radiologic appearances and differential diagnosis. *Radiographics*, 24:985–997, 2004.

[25] Stefan L.S. Kwa, Joos V. Lebesque, Jacqueline C.M. Theuws, Lawrence B. Marks, Mike T. Munley, Gunilla Bentel, Dieter Oetzel, Uwe Spahn, Mary V. Graham, Robert E. Drzymala, James A. Purdy, Allen S.

Lichter, Mary K. Martel, and Randall K. Ten Haken. Radiation pneumonitis as a function of mean lung dose: an analysis of pooled data of 540 patients. *International Journal of Radiation Oncology*Biology*Physics*, 42(1):1 – 9, 1998. ISSN 0360-3016.

[26] G Bisson, G Drapeau, G Lamoreux, A Cantin, M Rola-Pleszczynski, and R Begin. Computer-based quantitative analysis of gallium-67 uptake in normal and diseased lung. *Chest*, 84:513–517, 1983.

[27] P.G Gibson, D.H Bryant, B Robinson, G McLennan, and S.N Breit. The role of bronchoalveolar lavage in the assessment of diffuse lung diseases. *Aus. NZ J. Med.*, 19:281–291, 1989.

[28] P.G Gibson, D.H Bryant, G.W Morgan, M Yeates, V Fernandez, R Penny, and S.N Breit. Radiation-induced lung injury: a hypersensitivity pneumonitis. *Ann Intern Med.*, 15:288–291, 1988.

[29] Joseph O Deasy and Issam El Naqa. Image-based modeling of normal tissue complication probability for radiation therapy. *Cancer Treat Res*, 139:215–56, 2008. ISSN 0927-3042.

[30] M. Roach, DR Gandara, HS Yuo, PS Swift, S Kroll, DC Shrieve, WM Wara, L Margolis, and TL Phillips. Radiation pneumonitis following combined modality therapy for lung cancer: analysis of prognostic factors. *J Clin Oncol*, 13(10):2606–2612, 1995.

[31] Syed H. Abid, Vikas Malhotra, and Michael Perry. Radiation-induced and chemotherapy-induced pulmonary injury. *Current Opinion on Oncology*, 13(4):242–248, 2001.

[32] R. Byhardt, C. Scott, W. Sause, B. Emami, R. Komaki, B. Fisher, J. Lee, and C. Lawton. 120 Response, toxicity, failure patterns and survival in five radiation therapy oncology group (RTOG) trials of sequential and/or concurrent chemotherapy (CT) and radiation therapy (RT) for locally

advanced non-small cell carcinoma of the lung (NSCLC). *International Journal of Radiation Oncology*Biology*Physics*, 39(2, Supplement 1): 195 – 195, 1997.

[33] Christina K. Haston, Michelle Begin, Genevieve Dorion, and Sean M. Cory. Distinct Loci Influence Radiation-Induced Alveolitis from Fibrosing Alveolitis in the Mouse. *Cancer Res*, 67(22):10796–10803, 2007.

[34] Mitchell S. Anscher, Feng-Ming Kong, and Randy L. Jirtle. The relevance of transforming growth factor [beta]1 in pulmonary injury after radiation therapy. *Lung Cancer*, 19(2):109 – 120, 1998. ISSN 0169-5002.

[35] Kim De Ruyck, Marc Van Eijkeren, Kathleen Claes, Rudy Morthier, Anne De Paepe, Anne Vral, Leo De Ridder, and Hubert Thierens. Radiation-induced damage to normal tissues after radiotherapy in patients treated for gynecologic tumors: Association with single nucleotide polymorphisms in XRCC1, XRCC3, and OGG1 genes and in vitro chromosomal radiosensitivity in lymphocytes. *International Journal of Radiation Oncology*Biology*Physics*, 62(4):1140 – 1149, 2005. ISSN 0360-3016.

[36] Madani I, De Ruyck K, Goeminne H, De Neve W, Thierens H, and Van Meerbeeck J. Predicting risk of radiation-induced lung injury. *Journal of Thoracic Oncology*, 2(9):864–874, 2007.

[37] Li Zhang, Ming Yang, Nan Bi, Mingjing Fang, Tong Sun, Wei Ji, Wen Tan, Lujun Zhao, Dianke Yu, Dongxin Lin, and Luhua Wang. ATM Polymorphisms Are Associated With Risk of Radiation-Induced Pneumonitis. *International Journal of Radiation Oncology*Biology*Physics*, In Press, Corrected Proof:–, 2010. ISSN 0360-3016.

[38] Andrew J. Hope, Patricia E. Lindsay, Issam El Naqa, James R. Alaly, Milos Vicic, Jeffrey D. Bradley, and Joseph O. Deasy. Modeling radiation pneumonitis risk with clinical, dosimetric, and spatial parameters. *International Journal of Radiation Oncology*Biology*Physics*, 65(1):112 – 124, 2006. ISSN 0360-3016.

[39] M. Yamada, S. Kudoh, K. Hirata, T. Nakajima, and J. Yoshikawa. Risk factors of pneumonitis following chemoradiotherapy for lung cancer. *European Journal of Cancer*, 34(1):71 – 75, 1998. ISSN 0959-8049.

[40] Alena Novakova-Jiresova, Peter van Luijk, Harry van Goor, Harm H. Kampinga, and Robert P. Coppes. Pulmonary Radiation Injury: Identification of Risk Factors Associated with Regional Hypersensitivity. *Cancer Res*, 65(9):3568–3576, 2005.

[41] Kenji Koga, Shizuo Kusumoto, Katsushi Watanabe, Kiyoshi Nishikawa, Kuniko Harada, and Hiroaki Ebihara. Age factor relevant to the development of radiation pneumonitis in radiotherapy of lung cancer. *International Journal of Radiation Oncology*Biology*Physics*, 14(2):367 – 371, 1988. ISSN 0360-3016.

[42] Maria L. Hernando, Lawrence B. Marks, Gunilla C. Bentel, Su-Min Zhou, Donna Hollis, Shiva K. Das, Ming Fan, Michael T. Munley, Timothy D. Shafman, Mitchell S. Anscher, and Pehr A. Lind. Radiation-induced pulmonary toxicity: a dose-volume histogram analysis in 201 patients with lung cancer. *International Journal of Radiation Oncology*Biology*Physics*, 51(3):650 – 659, 2001. ISSN 0360-3016.

[43] J. M. Monson, P. Stark, J. J. Reilly, D. J. Sugarbaker, G. M. Strauss, S. J. Swanson, M. M. Decamp, S. J. Mentzer, and E. H. Baldini. Clinical radiation pneumonitis and radiographic changes after thoracic radiation therapy for lung carcinoma. *Cancer*, 82:842–850, 1998.

[44] Gerald J. Kutcher and C. Burman. Calculation of complication probability factors for non-uniform normal tissue irradiation: the effective volume method. *International Journal of Radiation Oncology*Biology*Physics*, 16(6):1623–1630, 1989.

[45] Mary Kaye Martel, Randall K. Ten Haken, Mark B. Hazuka, Andrew T. Turrisi, Benedick A. Fraass, and Allen S. Lichter. Dose-volume histogram and 3-d treatment planning evaluation of patients with pneumonitis. *International Journal of Radiation Oncology*Biology*Physics*, 28(3):575 – 581, 1994. ISSN 0360-3016.

[46] Dieter Oetzel, Peter Schraube, Frank Hensley, Gabriele Sroka-Prez, Markus Menke, and Michael Flentje. Estimation of pneumonitis risk in three-dimensional treatment planning using dose-volume histogram analysis. *International Journal of Radiation Oncology*Biology*Physics*, 33(2):455 – 460, 1995. ISSN 0360-3016.

[47] Mary V. Graham, James A. Purdy, Bahman Emami, William Harms, Walter Bosch, Mary Ann Lockett, and Carlos A. Perez. Clinical dose-volume histogram analysis for pneumonitis after 3D treatment for non-small cell lung cancer (NSCLC). *International Journal of Radiation Oncology*Biology*Physics*, 45(2):323 – 329, 1999.

[48] George Rodrigues, Michael Lock, David D'Souza, Edward Yu, and Jake Van Dyk. Prediction of radiation pneumonitis by dose-volume histogram parameters in lung cancer–a systematic review. *Radiotherapy and Oncology*, 71(2):127 – 138, 2004. ISSN 0167-8140.

[49] Issam El Naqa, Jeffrey Bradley, Angel I. Blanco, Patricia E. Lindsay, Milos Vicic, Andrew Hope, and Joseph O. Deasy. Multivariable modeling of radiotherapy outcomes, including dose-volume and clinical factors. *International Journal of Radiation Oncology*Biology*Physics*, 64(4):1275

– 1286, 2006. ISSN 0360-3016.

[50] D.W Hosmer and S Lemeshow. *Applied Logistic Regression*. John Wiley, 2000.

[51] Anders Ahnesjo and Maria Mania Aspradakis. Dose calculations for external photon beams in radiotherapy. *Physics in Medicine and Biology*, 44(11):R99, 1999.

[52] Indrin J. Chetty, Bruce Curran, Joanna E. Cygler, John J. DeMarco, Gary Ezzell, Bruce A. Faddegon, Iwan Kawrakow, Paul J. Keall, Helen Liu, C.-M. Charlie Ma, D. W. O. Rogers, Jan Seuntjens, Daryoush Sheikh-Bagheri, and Jeffrey V. Siebers. Report of the AAPM Task Group No. 105: Issues associated with clinical implementation of Monte Carlo-based photon and electron external beam treatment planning. *Medical Physics*, 34(12):4818–4853, 2007.

[53] Derek L.G. Hill, Philipp G. Batchelor, Mark Holden, and David J. Hawkes. Medical image registration. *Phys. Med. Biol.*, 46:R1–R45, 2001.

[54] D. L. Collins, P. Neelin, T. M. Peters, and A. C. Evans. Automatic 3D intersubject registration of MR volumetric data in standardized Talairach space. *J Comput Assist Tomogr*, 18(2):192–205, 1994. ISSN 0363-8715.

[55] P. A. van den Elsen, E. J. D. Pol, and M. A. Viergever. Medical image matching-a review with classification. *Engineering in Medicine and Biology Magazine, IEEE*, 12(1):26–39, 1993.

[56] J. Maintz and M. Viergever. A survey of medical image registration. *Medical Image Analysis*, 2(1):1–36, 1998.

[57] Joseph V. Hajnal, David J. Hawkes, and Derek L.G. Hill. *Medical Image Registration*. CRC press, 2001.

[58] W. R. Crum, T. Hartkens, and D. L. G. Hill. Non-rigid image registration: theory and practice. *Br J Radiol*, 77(2):S140–153, 2004.

[59] David Lowe. Object recognition from local scale-invariant features. In *International Conference on Computer Vision*, pages 1150–1157, 1999.

[60] K Rohr, H.S Stiehl, R Sprengel, T.M Buzug, J Weese, and M.H Kuhn. Landmark-based elastic registration using approximating thin-plate splines. *IEEE transactions on medical imaging*, 20(6):526–534, 2001.

[61] G.L. Hart, C. Zach, and M. Niethammer. An optimal control approach for deformable registration. *Computer Vision and Pattern Recognition Workshop*, 0:9–16, 2009.

[62] B.K.P Horn and B.G Schunck. Determining optical flow. *Artificial intelligence*, 17:185–203, 1981.

[63] J.-P. Thirion. Image matching as a diffusion process: an analogy with maxwell's demons. *Medical Image Analysis*, 2(3):243 – 260, 1998. ISSN 1361-8415.

[64] Ruzena Bajcsy and Stane Kovačič. Multiresolution elastic matching. *Comput. Vision Graph. Image Process.*, 46(1):1–21, 1989. ISSN 0734-189X.

[65] R. P. Woods, S. R. Cherry, and J. C. Mazziotta. Rapid automated algorithm for aligning and reslicing PET images. *Journal of Computer Assisted Tomography*, 16:620–633, 1992.

[66] Colin Studholme, Derek L. G. Hill, and David J. Hawkes. Automated three-dimensional registration of magnetic resonance and positron emission tomography brain images by multiresolution optimization of voxel similarity measures. *Medical Physics*, 24(1):25–35, 1997.

[67] Jocasta Webb, Alexandre Guimond, Paul Eldridge, David Chadwick, Jean Meunier, Jean-Philippe Thirion, and Neil Roberts. Automatic detection of hippocampal atrophy on magnetic resonance images. *Magnetic Resonance Imaging*, 17(8):1149 – 1161, 1999. ISSN 0730-725X.

[68] Martha M. Coselmon, James M. Balter, Daniel L. McShan, and Marc L. Kessler. Mutual information based CT registration of the lung at exhale and inhale breathing states using thin-plate splines. *Medical Physics*, 31 (11):2942–2948, 2004.

[69] K. M. Brock, J. M. Balter, L. A. Dawson, M. L. Kessler, and C. R. Meyer. Automated generation of a four-dimensional model of the liver using warping and mutual information. *Medical Physics*, 30(6):1128–1133, 2003.

[70] Julia A. Schnabel, Daniel Rueckert, Marcel Quist, Jane M. Blackall, Andy D. Castellano-Smith, Thomas Hartkens, Graeme P. Penney, Walter A. Hall, Haiying Liu, Charles L. Truwit, Frans A. Gerritsen, Derek L. G. Hill, and David J. Hawkes. A generic framework for non-rigid registration based on non-uniform multi-level free-form deformations. In *MICCAI '01: Proceedings of the 4th International Conference on Medical Image Computing and Computer-Assisted Intervention*, pages 573–581, London, UK, 2001. Springer-Verlag. ISBN 3-540-42697-3.

[71] D. Rueckert, L.I. Sonoda, C. Hayes, D.L.G. Hill, M.O. Leach, and D.J. Hawkes. Nonrigid registration using free-form deformations: application to breast MR images. *Medical Imaging, IEEE Transactions on*, 18(8): 712 –721, aug. 1999. ISSN 0278-0062.

[72] Thomas Guerrero, Geoffrey Zhang, Tzung-Chi Huang, and Kang-Ping Lin. Intrathoracic tumour motion estimation from CT imaging using the 3D optical flow method. *Physics in Medicine and Biology*, 49(17):

4147, 2004.

[73] Weiguo Lu, Gustavo H Olivera, Quan Chen, Kenneth J Ruchala, Jason Haimerl, Sanford L Meeks, Katja M Langen, and Patrick A Kupelian. Deformable registration of the planning image (kVCT) and the daily images (MVCT) for adaptive radiation therapy. *Physics in Medicine and Biology*, 51(17):4357, 2006.

[74] Authur W. Toga. *BRAIN WARPING*. Academic Press, 1998.

[75] Jeongtae Kim and J.A. Fessler. Intensity-based image registration using robust correlation coefficients. *Medical Imaging, IEEE Transactions on*, 23(11):1430 –1444, nov. 2004. ISSN 0278-0062.

[76] Michel A. Audette, Frank P. Ferrie, and Terry M. Peters. An algorithmic overview of surface registration techniques for medical imaging. *Medical Image Analysis*, 4(3):201 – 217, 2000. ISSN 1361-8415.

[77] C. E. Shannon. A mathematical theory of communication. *Bell System Technical Journal*, 27:379–423,623–656, 1948.

[78] C. Studholme, D. L. G. Hill, and D. J. Hawkes. An overlap invariant entropy measure of 3d medical image alignment. *Pattern Recognition*, 32(1):71 – 86, 1999. ISSN 0031-3203.

[79] André Collignon, Dirk Vandermeulen, Paul Suetens, and Guy Marchal. 3D Multi-Modality Medical Image Registration Using Feature Space Clustering. In *CVRMed '95: Proceedings of the First International Conference on Computer Vision, Virtual Reality and Robotics in Medicine*, pages 195–204, London, UK, 1995. Springer-Verlag. ISBN 3-540-59120-6.

[80] Paul Viola and William M. Wells, III. Alignment by maximization of mutual information. *Int. J. Comput. Vision*, 24(2):137–154, 1997. ISSN 0920-5691.

[81] C. Studholme, D. L. G. Hill, and D. J. Hawkes. Automated 3d registration of truncated mr and ct images of the head. In *BMVC '95: Proceedings of the 1995 British conference on Machine vision (Vol. 1)*, pages 27–36, Surrey, UK, UK, 1995. BMVA Press. ISBN 0-9521898-2-8.

[82] B tar Haar Romeny, L. M Florack, J. J Koenderink, and M. A Viergever. *Information Processing in Medical Imaging*. Springer Berlin/Heidelberg, 1991.

[83] N. M. Alpert, J. F. Bradshaw, D. Kennedy, and J. A. Correia. The Principal Axes Transformation–A Method for Image Registration. *J Nucl Med*, 31(10):1717–1722, 1990.

[84] D. Louis Collins and Alan C. Evans. Animal: Validation and Applications of Nonlinear Registration-Based Segmentation. *Int J Pattern Recognition Artificial Intelligences*, 11(8):1271–1294, 1997.

[85] Arnaud Charil, Alex P Zijdenbos, Jonathan Taylor, Cyrus Boelman, Keith J Worsley, Alan C Evans, and Alain Dagher. Statistical mapping analysis of lesion location and neurological disability in multiple sclerosis: application to 452 patient data sets. *NeuroImage*, 19(3):532 – 544, 2003. ISSN 1053-8119.

[86] Enzinger C, Smith S, Fazekas F, Drevin G, Ropele S, Nichols T, Behrens T, Schmidt R, and Matthews P.M. Lesion probability maps of white matter hyperintensities in elderly individuals: Results of the austrian stroke prevention study. *Journal of Neurology*, 253:1064–1070, 2006.

[87] SJ Thomas. Relative electron density calibration of CT scanners for radiotherapy treatment planning. *Br J Radiol*, 72(860):781–786, 1999.

[88] D. R. White, H. Q. Woodard, and S. M. Hammond. Average soft-tissue and bone models for use in radiation dosimetry. *Br J Radiol*, 60(717): 907–913, 1987.

[89] J. Sievinen, W. Ulmer, and W. Kaissl. AAA photon dose calculation in Eclipse. Technical Report documentation RAD 7170B, Varian, 2005.

[90] Ann Van Esch, Laura Tillikainen, Jukka Pyykkonen, Mikko Tenhunen, Hannu Helminen, Sami Siljamaki, Jyrki Alakuijala, Marta Paiusco, Mauro Iori, and Dominique P. Huyskens. Testing of the analytical anisotropic algorithm for photon dose calculation. *Medical Physics*, 33 (11):4130–4148, 2006.

[91] D. W. O. Rogers and A. F. Bielajew. *Monte Carlo techniques of electron and photon transport for radiation dosimetry*, chapter 5. Academic Pr., 1990.

[92] I. Kawrakow and D. W. O. Rogers. The egsnrc code system: Monte carlo simulation of electron and photon transport. Technical report, Technical Report PIRS-701, National Research Council of Canada, Ottawa, Canada, 2000.

[93] A Alexander, F DeBlois, G Stroian, K Al-Yahya, E Heath, and J Seuntjens. MMCTP: a radiotherapy research environment for Monte Carlo and patient-specific treatment planning. *Physics in Medicine and Biology*, 52(13):N297, 2007.

[94] D. W. O. Rogers, B. A. Faddegon, G. X. Ding, C.-M. Ma, J. We, and T. R. Mackie. BEAM: A Monte Carlo code to simulate radiotherapy treatment units. *Medical Physics*, 22(5):503–524, 1995.

[95] Fady B Geara, Ritsuko Komaki, Susan L Tucker, Elizabeth L Travis, and James D Cox. Factors influencing the development of lung fibrosis after chemoradiation for small cell carcinoma of the lung: Evidence for inherent interindividual variation. *International Journal of Radiation Oncology*Biology*Physics*, 41(2):279 – 286, 1998. ISSN 0360-3016.

[96] Ellen D. Yorke, Andrew Jackson, Kenneth E. Rosenzweig, Scott A. Merrick, Dorota Gabrys, Ennapadam S. Venkatraman, Chandra M. Burman, Steven A. Leibel, and C. Clifton Ling. Dose-volume factors contributing to the incidence of radiation pneumonitis in non-small-cell lung cancer patients treated with three-dimensional conformal radiation therapy. *International Journal of Radiation Oncology*Biology*Physics*, 54(2):329 – 339, 2002. ISSN 0360-3016.

[97] Katrien De Jaeger, Mischa S Hoogeman, Martijn Engelsman, Yvette Seppenwoolde, Eugene M.F. Damen, Ben J Mijnheer, Liesbeth J Boersma, and Joos V Lebesque. Incorporating an improved dose-calculation algorithm in conformal radiotherapy of lung cancer: re-evaluation of dose in normal lung tissue. *Radiotherapy and Oncology*, 69(1):1–10, 2003.

[98] Lawrence B. Marks, Xiaoli Yu, Zjelko Vujaskovic, William Small, Rodney Folz, and Mitchell S. Anscher. Radiation-induced lung injury. *Seminars in Radiation Oncology*, 13(3):333 – 345, 2003. ISSN 1053-4296.

[99] Andrzej Niemierko and Michael Goitein. Modeling of normal tissue response to radiation: The critical volume model. *International Journal of Radiation Oncology*Biology*Physics*, 25(1):135 – 145, 1993. ISSN 0360-3016.

[100] Zhong-Xing Liao, Elizabeth L. Travis, and Susan L. Tucker. Damage and morbidity from pneumonitis after irradiation of partial volumes of mouse lung. *International Journal of Radiation Oncology*Biology*Physics*, 32 (5):1359 – 1370, 1995. ISSN 0360-3016.

[101] Zafer Kocak, Lalitha Shankar, Daniel C. Sullivan, and Lawrence B. Marks. The Role of Imaging in the Study of Radiation-Induced Normal Tissue Injury. In L. W. Brady, H. P. Heilmann, M. Molls, C. Nieder,

Philip Rubin, Louis S. Constine, Lawrence B. Marks, and Paul Okunieff, editors, *Late Effects of Cancer Treatment on Normal Tissues*, Medical Radiology, pages 37–45. Springer Berlin Heidelberg, 2008.

[102] Lawrence B. Marks, Soren M. Bentzen, Joseph O. Deasy, Feng-Ming Kong, Jeffrey D. Bradley, Ivan S. Vogelius, Issam El Naqa, Jessica L. Hubbs, Joos V. Lebesque, Robert D. Timmerman, Mary K. Martel, and Andrew Jackson. Radiation dose-volume effects in the lung. *International Journal of Radiation Oncology*Biology*Physics*, 76(3, Supplement 1):S70 – S76, 2010. ISSN 0360-3016. Quantitative Analyses of Normal Tissue Effects in the Clinic.